UNIVERSITY OF CALIFORNIA SAN DIEGO

A Numerical Study on Elliptical Instabilities in a Counter-Rotating Asymmetric Vortex Pair

A thesis submitted in partial satisfaction of the requirements
for the degree Master of Science

in

Mechanical Engineering

by

Doris Stumps

Committee in charge:

Professor Keiko Nomura, Chair
Professor Antonio Sanchez
Professor David Saintillan

2023

The dissertation of Doris Stumps is approved, and it is acceptable in quality and form for publication on microfilm and electronically.

University of California San Diego

2023

TABLE OF CONTENTS

LIST OF FIGURES

LIST OF TABLES

ACKNOWLEDGEMENTS

I would like to thank my advisor, Professor Keiko Nomura, for encouraging me to take part in the graduate program, and for providing invaluable guidance, resources, and insights along the way. I would also like to thank Professor Antonio Sanchez and Professor David Saintillan for serving as my thesis committee members and providing valuable suggestions for future works.

I'm grateful to my fellow graduate students for all the helpful suggestions and conversations. Reiley Weekes introduced me to Nek5000, the CFD code that I used to perform my simulations, and he helped set up the servers in our CFD lab. The discussions we had regarding Nek5000 helped me greatly in my coding endeavors. Scott Carlson and Patrick Foltz have assisted me with their suggestions on research topics as well as advice on field initialization and many other aspects of CFD.

Finally, I would like to thank my boyfriend, my parents, and my friends for all the emotional support and words of encouragement they have given me during this journey. They have been so patient and understanding throughout my time in the graduate program and I couldn't have done it without them.

ABSTRACT OF THE THESIS

A Numerical Study on Elliptical Instabilities in a Counter-Rotating Asymmetric Vortex Pair

by

Doris Stumps

Master of Science in Mechanical Engineering

University of California San Diego, 2023

Professor Keiko Nomura, Chair

The elliptical instability in two unequal counter rotating vortices is studied with numerical simulations for a circulation Reynolds number of Re_Γ =3100. The initially Gaussian vortices with equal and opposite circulation but unequal peak vorticity and core size are subjected to random perturbations, and their time evolution in the linear phases is examined.

Asymmetry is achieved by simultaneously increasing core radius and lowering peak vorticity on one vortex while keeping the properties on the other vortex fixed between simulations.

The effects of this asymmetry on the interaction between the two vortices are then studied, and it is found that deformation is more prominent on the larger vortex with lower peak vorticity for all simulations due to the higher relative strain it experiences. The most unstable non-dimensional wavenumber increases for increasingly asymmetrical cases; the global growth rate of the most unstable mode is higher in the weakly asymmetrical pair than the symmetrical pair and the strongly asymmetrical pair.

Chapter I Introduction

Two initially counter-rotating and parallel vortices may interact and become unstable, resulting in three-dimensional deformation and eventual breakdown of the vortex cores. The subject of this study is the elliptical instability of two counter-rotating and unequal vortices. In this chapter, motivation for this study along with some background and previous work are presented. The objectives of this research are then given, followed by an outline for the rest of the thesis.

I.A Motivation

The nature and growth of instabilities between two counter-rotating vortices have long been a topic of practical significance. In aeronautics, the strong counter-rotating wingtip vortices generated by heavy aircrafts can be hazardous to smaller aircraft that follow too closely. Since they can induce rolling and loss of altitude, minimum flight separation distances between successive aircraft takeoffs and landings are thus implemented to avoid such encounters [1]. The development of 3D instabilities between the wingtip vortices, which are often observed behind aircrafts at high altitudes due to moisture condensing in the vortex cores, can accelerate the destruction of the vortices and shorten the separation distance needed, better optimizing air traffic.

In addition to the primary wing tip vortices, weaker vortices may be generated from other surfaces on the aircraft such as wing flaps and stabilators and interact with the wingtip vortex on their respective sides; the growth of the unstable perturbations during these interactions between unequal vortices can further catalyze vortex destruction [2]. In fact, in most real-world applications, interacting vortices are often unequal in certain aspects due to the variability of the surfaces from which they are shed. Thus, it is of practical interest to study the development of instabilities and subsequent evolution of unequal vortices. As discussed in the next section, majority of the existing studies consider equal strength vortices, so the objective of this study is to

expand on existing investigations about three-dimensional instabilities—more specifically the elliptical instability, which is discussed in more detail below—between unequal counter-rotating vortex pairs.

I.B Literature Review

Numerous analytical, experimental, and numerical studies have been carried out on the interaction between two counter-rotating vortices. In the first systematic studies on the wingtip vortices by [3], [4], and [5], it is found that both a long-wave instability, the Crow instability, and a short-wave instability, the elliptical instability, can develop during such interactions.

In the following sections, background and relevant work on these instabilities in both equal and unequal counter-rotating (opposite-sign) vortex pairs are presented, where an *equal* vortex pair refers to two vortices having the same circulation magnitude, core size, and vorticity distribution, and an *unequal* pair refers to two vortices with differences in one or more of these parameters.

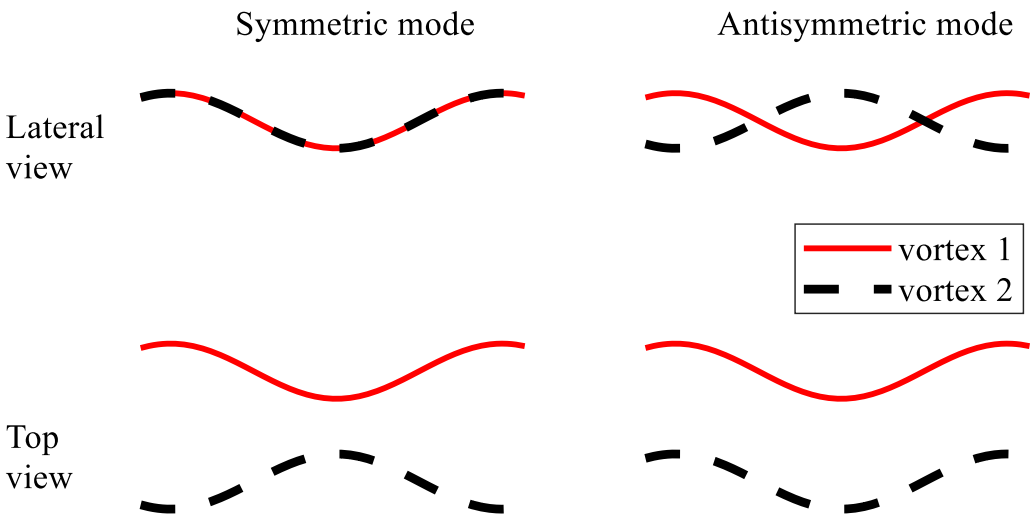

Figure I.1: Qualitative schematic of symmetric and antisymmetric modes (not to scale).

I.B.1 Equal Vortex Pair

Long-wave Instability

The long-wave instability, also known as the Crow instability, can only develop on a counter-rotating vortex pair and not a co-rotating (same-sign) vortex pair. In this instability, the vortices experience a three-dimensional, sinusoidal displacement that is symmetrical with respect to the midplane between them (Figure I.1: symmetric mode); the perturbation grows on a plane inclined approximately 45° away from the midplane, displacing vortices without resulting in any changes to their internal core structure. This instability was first theoretically formulated by Crow [3] using linear stability analysis. Two equal and counter-rotating vortices are approximated as interacting vortex lines; their mutual inductance is calculated with the Biot-Savart Law while self-inductance is similarly calculated but with the application of a cutoff distance method. Assuming the vortices have a small core size relative to the separation distance and a uniform vorticity profile, Crow calculated that the long-wave instability has the most unstable wavelength of $8.6b_0$, b_0 being the initial separation distance between the vortices. When the vortices are modelled with a finite core size, this wavelength is found to range between 6 to $10b_0$, depending on the ratio of the core size and vortex separation [6]. Widnall et al [7] and Moore and Saffman [8] generalized these linear stability theories to vortices with nonuniform vorticity profiles and nonzero axial flow. This long-wave instability was also noted in experimental observations and numerical studies, including the nonlinear stage of the instability with the eventual reconnection of the vortex pair into a series of vortex rings [9, 10]. Further studies investigated the nonlinear stage of Crow instability and the vortex reconnection phenomenon [9], taking into account parameters such as the scale of ambient turbulence [11, 12] and stratification [13].

Short-wave Instability

In his work, Crow also discussed the presence of two instability modes with higher wavenumber than the classic Crow mode; though [4] later showed that this was only a spurious instability due to the invalid usage of the long wave asymptotic analysis on shortwaves for self-induced rotation, they also found that another antisymmetric short-wave mode with a more complex radial structure exists. This short-wave instability is the so-called elliptical instability since it develops in regions with elliptical streamlines [14, 15]. The perturbation flow generated by this instability is characterized by an axial wavelength on the same scale as the core size of the vortex, as well as distorted vortex core structure and displaced vortex centers [15]. The instability is the result of resonant coupling between a strain field and Kelvin modes that are otherwise neutral on an unstrained vortex; when there is a single vortex, the perturbation rotates due to the self-induced velocity field, but when in the presence of another vortex, the self-rotation for certain perturbation wavelengths is balanced out by the induced velocity from the strain field, and the perturbation amplifies radially on a plane inclined 45° from the axis that connects the two vortex centers [4, 6, 14, 2, 10], with a linear growth rate that scales with the strain rate [14]. Therefore, the closer the vortices are to each other, the higher the growth rate of the perturbation due to the increased strain induced by each vortex on the other. In the nonlinear regime, the perturbation amplitude is no longer small compared to the base flow, and the amplified perturbation modes become detuned from the 45° plane they were growing on [16]. The displaced vortex cores draw opposite-signed vorticity from the other vortex, forming transverse vorticity bridges that are counter-rotating along the length of the initial vortex pair, see [15]. The process repeats on a smaller scale until the breakdown of the vortex pair is reached.

There also exists an interaction between the long-wave and short-wave instabilities, which affects the long-term development of the aircraft wake. As seen in the experiments by Leweke and Williamson [6] and the subsequent direct numerical simulation (DNS) study by Laporte and Corjon [10], when the vortex pair is far apart, long-wave modes dominate and the symmetric perturbation causes the vortices to come closer together at periodic intervals along the axial direction; elliptical instability develops more rapidly at these locations, leading to vortex reconnection as previously mentioned. It is also concluded in [10] that the development of both instabilities in the flow are dependent on the initial amount of kinetic energy existing in the corresponding instability modes.

I.B.2 Unequal Vortex Pair

In comparison to the instabilities between a pair of equal strength vortices, those that occur in an unequal pair are more complex due to the asymmetry of the flow and the increased number of parameters involved. In the DNS study of So et al [17], the growth rate of both the long and short-wave instabilities are studied on unequal pairs with $-1 \leq \Lambda \leq -0.1$, achieved by considering equal core size and varying the peak vorticity of the vortices. With circulation Reynolds number of 20,000 and aspect ratio a/b of approximately 0.27, the two circular Lamb Oseen vortices are initialized and evolve in a two-dimensional domain until they adapt to the external strain field generated by each other, then they are allowed to develop in three dimensions. It was found that while the short-wave Kelvin modes grow preferentially on the weaker vortex, leaving the stronger vortex mostly unaffected, the Crow instability grows on both with higher growth rate and wavenumber as the pair becomes increasingly unequal until a critical circulation ratio, beyond which the growth rate decreases again. The result of Crow instability developing in unequal pairs with higher growth rate and wavenumber is validated by the linear stability analysis done in Bristol

et al [2] as well as the experimental work of Ortega et al [18], though the decrease in growth rate for severely unequal vortices was not observed in the analytical study, possibly due to the limitations of the linear model of the instability. Bristol et al [2] also noted that the Crow growth rate only weakly depends on aspect ratio of the vortex pair, which, per the interaction between long-wave and short-wave instabilities discussed earlier, assist with the rapid onset of short-wave instability even in unequal vortex pairs with initially high aspect ratios. The findings from So et al [17] regarding the short-wave instability are supported by the theoretical work done by Le Dizès & Laporte [19]. Specifically, the theoretical model presented in [19] predicts the growth rate of the elliptical instability for a vortex pair with arbitrary circulation and core sizes; this theoretical model has been shown to provide excellent estimates for flows with high Reynolds number ($Re_\Gamma > 10^5$) and low aspect ratio ($a/b < 0.18$), but limited accuracy for flows that fall outside of these parameter ranges.

I.C Objectives of the Study

The objective of this study is to further investigate the behavior of the elliptical instabilities in an unequal vortex pair with asymmetries in both peak vorticity and core size, in particular, the case in which the circulation magnitudes of the vortices are equal is considered. This is done to isolate the effects of the aforementioned parameters, excluding that of unequal circulation on the instability growth behavior. In all the previous studies, the vortex with smaller circulation magnitude of the unequal pair is found to experience greater deformation due to the relatively larger external strain acting on it from the stronger vortex. These studies varied the peak vorticity of the pair while keeping the core size of the vortices equal, so it is always apparent which of the two unequal vortices is the weaker one and would be the first to display signs of deformation. However, when the circulation magnitudes are comparable in the unequal pair, it is not clear how

to generalize the results of the previous studies to this case to determine whether the instability would grow more rapidly on one vortex or the other, or that the theoretical prediction model from [19] can be readily applied. A numerical study is conducted to investigate the influence of core size and peak vorticity on the instabilities, because it allows for easier control and alteration of these specific parameters than in an experimental setting, it also offers more flexibility than theoretical models that are only accurate when certain assumptions are fulfilled.

The thesis is outlined as follows. In Chapter 2, the physical flow, mathematical formulation, and simulations are described. In Chapter 3 and 4, results from the simulations are presented and discussed. In the final Chapter, a summary of the current study and possible future work are provided.

Chapter II Numerical Simulation

In this chapter, the vortex pair being studied is described. The important flow parameters and governing equations are then presented, followed by the numerical formulation and numerical methods employed in this DNS study.

II.A Flow Description

A pair of counter-rotating vortices in viscous, incompressible flow is considered. The pair is initialized as the superposition of two axisymmetric Lamb-Oseen vortices that have equal circulation magnitude, $|\Gamma_{01}| = |\Gamma_{02}| = \Gamma_0 = |\omega_{0,i}|\pi a_{0,i}^2$, but unequal core radii, $a_{0,i}$, and peak vorticity magnitudes, $|\omega_{0,i}|$; the subscript 0 hereafter denotes the parameter values associated with the initial condition. The two vortices are initially separated by a peak-to-peak distance of b_0. A graphical representation of this initial flow with random perturbations can be seen in Figure II.1. Subjected to small velocity perturbations, the vortex pair experiences temporal evolution in three dimensions due to the elliptical instability mechanism acting on and amplifying these perturbations to the base flow field.

To simplify the problem, factors such as stratification, axial flow, and the existence of additional vortices from the wingtip roll-up process are not considered in this case despite their presence in practical applications. The domain size and the initial condition are also specifically designed to prevent the onset of the Crow instability in this study, the details of which are discussed in the following sections.

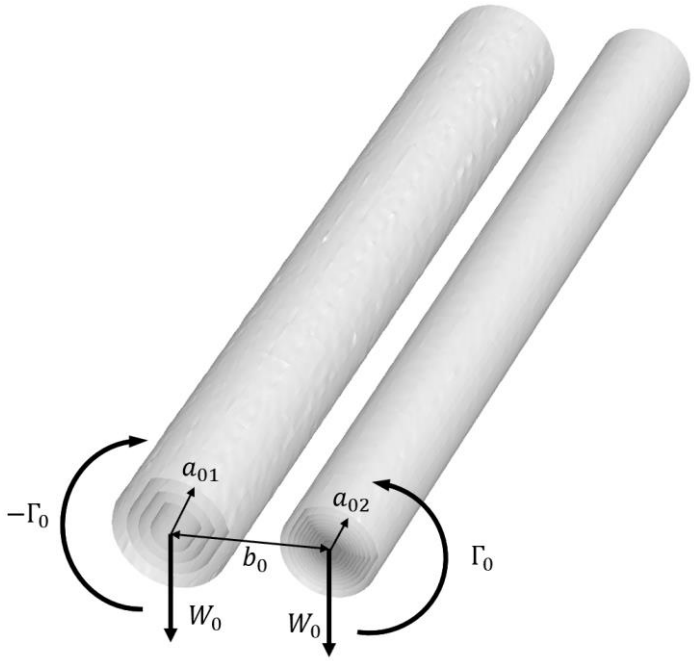

Figure II.1: An unequal pair of counter-rotating vortices with same circulation magnitude but different core sizes.

II.B Flow Parameters

With the aforementioned simplifications, the vortical fluid motion from the vortex pair—the strength of which is measured by circulation—is the sole contributor of inertial forces within the flow. The circulation Reynolds number, defined as

$$Re_{\Gamma} = \frac{\Gamma_0}{\nu} \qquad \text{Eq. II-1}$$

can be used to quantify the relative significance between the inertial and viscous forces in the flow; here, ν is the kinematic viscosity of the fluid.

Given the circulation and core size, the peak vorticity of each Lamb-Oseen vortex can be determined by

$$\omega_{0,i} = \frac{\Gamma_0}{\pi a_{0,i}^2} \qquad \text{Eq. II-2}$$

The flow can be characterized by the length scale b_0 and the velocity scale W_0. As shown in Figure II.1, b_0 is the separation distance between the two vortex centers, and W_0 is the speed at which the vortices are advected downwards by each other. W_0 is proportional to the circulation magnitude, Γ_0, specifically:

$$W_0 = \frac{\Gamma_0}{2\pi b_0} \qquad \text{Eq. II-3}$$

The characteristic time scale, T_0, is defined by

$$T_0 = \frac{b_0}{W_0} \qquad \text{Eq. II-4}$$

This can be thought of as the time it takes for the pair to propagate downwards by a distance b_0.

In this study, all simulations have a circulation Reynolds number, Re_Γ, of 3100, and the two vortices have initial circulation ratio, $\frac{\Gamma_{01}}{\Gamma_{02}}$, of -1 to ensure they are initialized as equal-strength counter-rotating vortices. The parameters of vortex 2 is fixed across all simulations and it has an aspect ratio, $\frac{a_{02}}{b_0}$, of 0.2. The parameters of vortex 1 changes between simulations such that the core size ratio, $\frac{a_{01}}{a_{02}}$, varies between 1 and 1.75, and the peak vorticity ratio varies such that $\frac{\omega_{02}}{\omega_{01}} = \left(\frac{a_{01}}{a_{02}}\right)^2$

II.C Governing Equations

The governing equations of the flow are the continuity equation and the Navier-Stokes equations.

The general form of the continuity equation, $\frac{\partial \rho}{\partial t} + \nabla \cdot (\rho \vec{v}) = 0$, with the assumption that the flow is incompressible, $\frac{D\rho}{Dt} = \frac{\partial \rho}{\partial t} + \vec{v} \cdot \nabla \rho = 0$, simplifies to:

$$\nabla \cdot \vec{v} = 0 \qquad \text{Eq. II-5}$$

Using the scaling from Table II.1 and dividing both sides by $\frac{W_0}{b_0}$, the equation above can be converted into its non-dimensional form (the * superscript denotes non-dimensional quantities):

$$\nabla^* \cdot \vec{v}^* = 0 \qquad \text{Eq. II-6}$$

The Navier-Stokes momentum equations in vector form, excluding body forces such as gravitational effects and buoyancy, for an incompressible flow with constant density and viscosity can be written as:

$$\rho \frac{\partial(\vec{v})}{\partial t} + \rho(\vec{v} \cdot \nabla)\vec{v} = -\nabla p + \mu \nabla^2 \vec{v} \qquad \text{Eq. II-7}$$

Eq. II-8 is obtained by non-dimensionalizing Eq. II-7 using the scaling in Table II.1.

$$\frac{\rho {W_0}^2}{b_0}\left(\frac{\partial(\vec{v}^*)}{\partial t^*} + (\vec{v}^* \cdot \nabla^*)\vec{v}^*\right) = \frac{\rho {W_0}^2}{b_0}\left(-\nabla^* p^* + \frac{\mu}{\rho W_0}\nabla^{*2}\vec{v}^*\right) \qquad \text{Eq. II-8}$$

Dividing both sides by $\frac{\rho {W_0}^2}{b_0}$, Eq. II-8 simplifies to the following non-dimensionalized Navier-Stokes momentum equation.

$$\frac{\partial(\vec{v}^*)}{\partial t^*} + (\vec{v}^* \cdot \nabla^*)\vec{v}^* = -\nabla^* p^* + \frac{2\pi}{\mathrm{Re}_\Gamma}\nabla^{*2}\vec{v}^* \qquad \text{Eq. II-9}$$

For all simulations, the value of Re_Γ is set to 3100 to ensure that the velocity field is well resolved for the number of gridpoints in the computational domain and that the Reynolds number is not a variable contributing to the differences between simulation results.

Table II.1: Non-dimensional variables

Velocity:	$\vec{v}^* = \frac{\vec{v}}{W_0}$	Pressure:	$p^* = \frac{p}{\rho {W_0}^2}$
Time:	$t^* = \frac{t W_0}{b_0}$	Del operator:	$\nabla^* = b_0 \nabla$

II.D Numerical Formulation

II.D.1 Computational Domain

The physical flow as described in Section II.A, is simulated in a rectangular computational domain in a Cartesian coordinate system as shown in Figure II.2. As indicated in the figure, x is the transverse direction, parallel to a line that would connect the two initial vortex centers, y is the vertical direction, and z is the axial direction. The domain has sides with length $L_x = 4\pi b_0$, $L_y = 6\pi b_0$, and $L_z = 2\pi b_0$, and is discretized into a non-uniform mesh that contains a number of elements that are further divided into a total of 420, 532 and 112 unique gridpoints respectively in each direction. The periodic boundary condition is used in all three directions, which is equivalent to the vortex pair being surrounded by identical vortex pairs in an unbounded domain.

The domain size is chosen specifically to avoid issues that may arise from the periodic boundary condition. The size of the domain in the axial direction has shown to affect the wavelength of the most amplified mode of the elliptical instability, unless the axial dimension of the bounding box is larger than 5 times the naturally most amplified wavelength [10]. However, the length of the axial domain also should be limited to minimize the chance for the Crow instability, which is typically $6b_0 - 10b_0$ [6], to develop. Since it is known a priori that the most amplified modes for elliptical instability have wavelengths on the same scale as the vortex core sizes, and that the core sizes for all simulations lie in the range of $0.2b_0 \leq a_{01,02} \leq 0.35b_0$, L_z is set to $2\pi b_0$. It is verified posteriori that the axial domain size is larger than 5 times the most unstable modes for all simulations, and thus, adequate for the purpose of this paper. In addition, due to the period boundary condition, the domain must be sufficiently large in the x direction to prevent the presence of the "surrounding vortex pairs" from having a significant impact on the development of the instabilities within the pair. While [10] and [16] had transverse domain length

of only $5b_0$ and $6b_0$, respectively, the runs in these studies also have lower circulation Reynolds numbers ($\mathrm{Re}_\Gamma = 2400$) as well as smaller vortex core sizes than the current study. Instead of optimizing the domain width for all simulations, $L_x = 4\pi b_0$ is picked to allow for ample spacing in the transverse direction and a non-uniform mesh is utilized to offset the higher computation cost from a larger domain (the non-uniform mesh and spatial discretization is further discussed in Section II.E.1). Furthermore, as the vortex pair propagates downwards, they exit out of the bottom of the domain and an identical pair re-enters from the top due to the periodic boundary condition. The height of the bounding box must be large enough to prevent the pair from traveling through its own wake during the linear growth phase of the elliptical instability, as the perturbed flow field in the wake could interact with the elliptical instability and impact the study. It's observed that for all simulations, the linear growth phase occurs well before the pair travels close to its own wake when $L_y = 6\pi b_0$. The linear growth rate result from a run with $L_y = 6\pi b_0$ is also compared against the results from another simulation with $L_y = 8\pi b_0$, and no significant difference is found in the growth rate and wavenumber of the most unstable mode. Therefore $L_y = 6\pi b_0$ is used for all simulations.

At the start of the simulations, the vortex pair is located in the middle of the computational domain, with each of their vortex centers at $(x_{c1}, y_{c1}) = (\frac{L_x - b_0}{2}, \frac{L_y}{2})$, and $(x_{c2}, y_{c2}) = (\frac{L_x + b_0}{2}, \frac{L_y}{2})$.

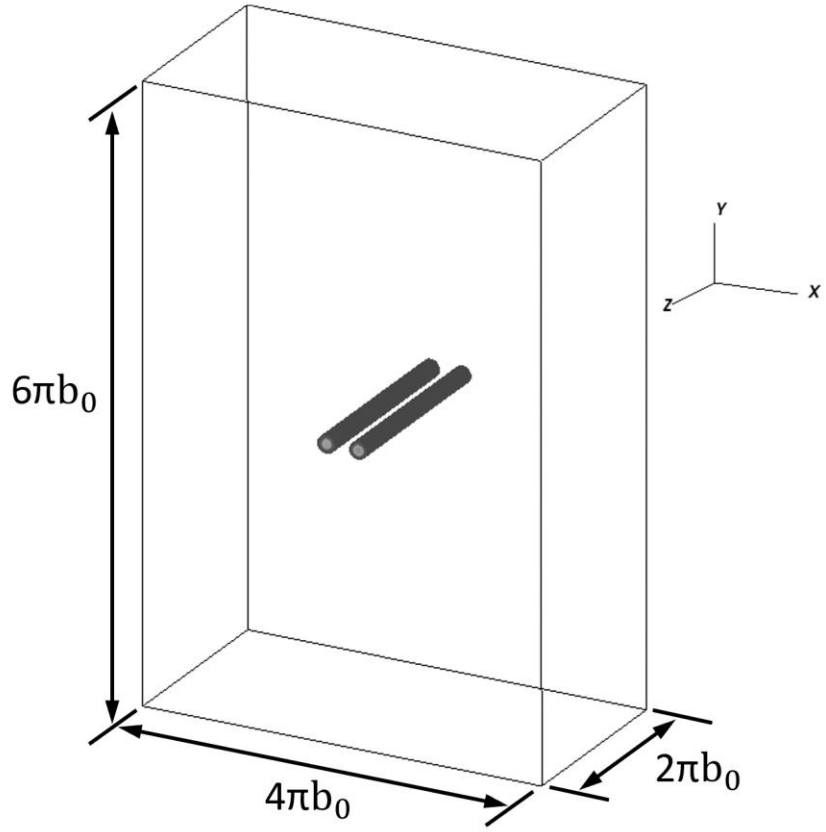

Figure II.2: Computational domain with Cartesian coordinate system

II.D.2 Initial Condition

The Lamb-Oseen vortex is chosen for the study because its Gaussian vorticity profile closely resembles the profiles of naturally occurring viscous vortices. In a flow influenced by the existence of a single Lamb-Oseen vortex, otherwise known as the Gaussian vortex, with motion confined to the x-y plane, the only non-zero component of the vorticity is in the z direction, as described by Eq. II-10 [6].

$$\omega_z(x,y) = \frac{\Gamma}{\pi a^2}\exp\left(-\frac{(x-x_c)^2+(y-y_c)^2}{a^2}\right) \qquad \text{Eq. II-10}$$

Superimposing the vorticity distributions from two counter-rotating, Lamb-Oseen vortices, the initial vorticity distribution is as shown in Eq. II-11. Here, uppercase Ω is used to indicate vorticity associated with the base flow in the study, without the presence of perturbations.

$$\Omega_{0z}(x,y) = \frac{-\Gamma_0}{\pi a_{01}^2}\exp\left(-\frac{(x-x_{c1})^2+(y-y_{c1})^2}{a_{01}^2}\right) + \frac{\Gamma_0}{\pi a_{02}^2}\exp\left(-\frac{(x-x_{c2})^2+(y-y_{c2})^2}{a_{02}^2}\right) \quad \text{Eq. II-11}$$

Applying the definition of vorticity, $\omega = \nabla \times u$, and the continuity equation, the initial base flow velocity distribution can be derived. Here, uppercase U is used to indicate vorticity associated with the base flow.

$$U_{0x}(x,y) = \frac{\Gamma_0(y-y_{c1})}{2\pi[(x-x_{c1})^2+(y-y_{c1})^2]}\left[1-\exp\left(-\frac{(x-x_{c1})^2+(y-y_{c1})^2}{a_{01}^2}\right)\right] - \frac{\Gamma_0(y-y_{c2})}{2\pi[(x-x_{c2})^2+(y-y_{c2})^2]}\left[1-\exp\left(-\frac{(x-x_{c2})^2+(y-y_{c2})^2}{a_{02}^2}\right)\right] \quad \text{Eq. II-12}$$

$$U_{0y}(x,y) = -\frac{\Gamma_0(x-x_{c1})}{2\pi[(x-x_{c1})^2+(y-y_{c1})^2]}\left[1-\exp\left(-\frac{(x-x_{c1})^2+(y-y_{c1})^2}{a_{01}^2}\right)\right] + \frac{\Gamma_0(x-x_{c2})}{2\pi[(x-x_{c2})^2+(y-y_{c2})^2]}\left[1-\exp\left(-\frac{(x-x_{c2})^2+(y-y_{c2})^2}{a_{02}^2}\right)\right] \quad \text{Eq. II-13}$$

$$U_{0z}(x,y) = 0 \quad \text{Eq. II-14}$$

It's important to note that the initial base velocity field obtained by superimposing two axisymmetric Lamb-Oseen vortices is not a solution of the Navier-Stokes equations [20, 10], as the vortices should have somewhat elliptical streamlines due to the strain they exert on each other. A transition period is required for these vortices to adapt to the induced strain field and become solutions to the Navier-Stokes equations. Different initial conditions can be used to shorten this adaptation period, such as the Lamb dipole suggested by Orlandi et al [21]. Since this viscous adaptation is shown to be purely two-dimensional and does not affect the growth of the three-dimensional instabilities [10], no steps have been specifically taken to eliminate this transition phase.

A white noise is then superimposed onto each of the three components of the base velocity field, creating the perturbations needed to trigger the elliptical instability. For all three components,

the positive or negative velocity perturbation generated at each gridpoint within the computational domain, $\tilde{u}_{x,y,z}$, has an amplitude no higher than 0.1% of the initial descent speed, W_0.

$$-0.001W_0 \leq \tilde{u}_{0x,0y,0z}(x,y,z) \leq 0.001W_0 \qquad \text{Eq. II-15}$$

The maximum perturbation amplitude is constrained as above to prevent the occurrence of large outliers that could lead to early onset of nonlinear dynamics. The white noise is also generated in a deterministic fashion based on the computational domain mesh that makes it repeatable while still being random. It was verified posteriori that the perturbation kinetic energy corresponding to the modes of the Crow instability is not preponderant in the white noise initial condition so that the long-wave instability is unlikely to develop [10]. No special steps have been taken to guarantee that the generated white noise is divergence-free. However, this is resolved during the first time-step of the simulation, where the pressure scalar field is solved in such a fashion to ensure that the velocity field in the new time step is divergence free. Thus, with the addition of the generated white noise, the initial velocity field is described by Eq. II-16-Eq. II-18.

$$u_{0x}(x,y,z) = \frac{\Gamma_0(y-y_{c1})}{2\pi[(x-x_{c1})^2+(y-y_{c1})^2]}\left[1-\exp\left(-\frac{(x-x_{c1})^2+(y-y_{c1})^2}{a_{01}^2}\right)\right] - \frac{\Gamma_0(y-y_{c2})}{2\pi[(x-x_{c2})^2+(y-y_{c2})^2]}\left[1-\exp\left(-\frac{(x-x_{c2})^2+(y-y_{c2})^2}{a_{02}^2}\right)\right] + \tilde{u}_{0x}(x,y,z) \qquad \text{Eq. II-16}$$

$$u_{0y}(x,y,z) = -\frac{\Gamma_0(x-x_{c1})}{2\pi[(x-x_{c1})^2+(y-y_{c1})^2]}\left[1-\exp\left(-\frac{(x-x_{c1})^2+(y-y_{c1})^2}{a_{01}^2}\right)\right] + \frac{\Gamma_0(x-x_{c2})}{2\pi[(x-x_{c2})^2+(y-y_{c2})^2]}\left[1-\exp\left(-\frac{(x-x_{c2})^2+(y-y_{c2})^2}{a_{02}^2}\right)\right] + \tilde{u}_{0y}(x,y,z) \qquad \text{Eq. II-17}$$

$$u_{0z}(x,y,z) = \tilde{u}_{0z}(x,y,z) \qquad \text{Eq. II-18}$$

II.E Numerical Method

The direct numerical simulation (DNS) code within the open-source computational fluid dynamics (CFD) solver Nek5000 is used to solve the Navier-Stokes equations. The spatial

discretization in the solver is based on the spectral element method (SEM) and the time-stepping is done using an implicit-explicit multistep method. The spatial discretization, temporal integration, and their respective resolutions in the context of this study are discussed in detail below. Specifics regarding the CFD solver Nek5000 can be found in [22].

II.E.1 Spatial Discretization and Resolution

The spatial discretization within the Nek5000 solver is based on the SEM; it combines the flexibility of the finite element method with high order of accuracy like those of spectral methods. Much like the finite element method, the domain is discretized into elements that can vary in size and shape. However, within each element, the velocity is approximated as an expansion of high order polynomial basis functions of order p with unknown coefficients at p+1 non-uniformly spaced Gauss-Lobatto-Legendre (GLL) collation points. The unknown coefficients for the basis functions are calculated using a weighted residual technique.

In the current study, the domain is discretized such that the elements are varying in size in the x direction only but have uniform sizing in the y and z directions. The elements are coarse near the transverse boundaries of the computational domain but becomes finer in the middle of the domain, as seen in the example mesh in Figure II.3. This is to ensure that the region through which the vortices propagate have high enough resolution to fully resolve the velocity gradients in the core of the vortices. This results in a total of 60 by 76 by 16 elements in the x, y, and z direction, respectively.

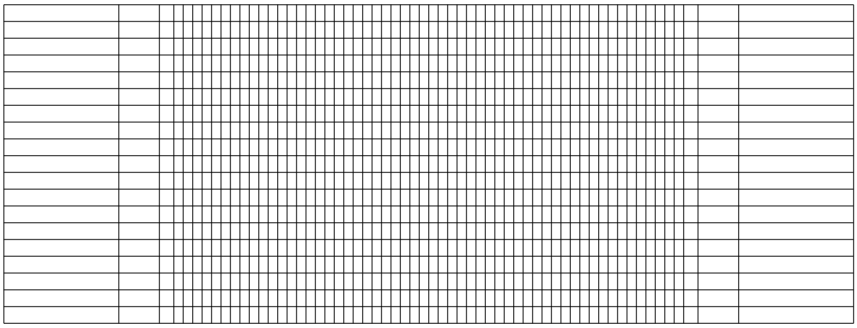

Figure II.3: Non-uniform mesh with varying element size in the x direction, 2D view

Using a 7^{th} order spectral element mesh, the velocity is solved at 8 GLL collation points within each element in each direction (Figure II.4). To maintain continuity between the elements and the numerical solutions, the collation points on the face of an element share the same location as the collation points from the neighboring element. This yields 7 distinct node locations in each direction for each element, for a total of 420 by 532 by 112 nodes in the spectral element mesh within the computational domain. There are approximately 12 nodes across the initial core size in the x direction, and 7 nodes in the y direction. This resolution was chosen because it has been shown in [10] that a grid slightly coarser than the one discussed has been sufficient for similar simulations. The current spatial resolution has also been confirmed to be sufficient to fully resolve the velocity scale within the simulated flow in the linear regime through comparing simulation results against one run with a finer grid. It's worth noting, however, as the 3D instabilities continue to develop in the nonlinear regime and break down the primary coherent structures of the vortices, the smaller scale flow structures as the result of secondary and tertiary vortices are not fully resolved at the current grid size (Figure II.5). As the goal of this study is to investigate the instability growth rate in the linear regime, the resolution at which the simulations are run are not refined further, so quantitative data in the linear flow can be gathered, analyzed, and compared across simulations without incurring the additional computational cost needed to fully resolve the

nonlinear flow. For the nonlinear regime, only the qualitative visualization results will be shown and discussed.

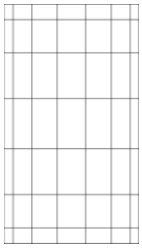

Figure II.4: GLL collation points within each element in each direction for a 7^{th} order spectral element mesh.

II.E.2 Time Stepping

The time marching in this study is done using a 3rd-order implicit-explicit multistep method that is built into Nek5000. The nonlinear convective terms in the Navier-Stokes equations are approximated using an explicit 3rd-order extrapolation method (EXT3) to prevent the need to solve for a nonlinear system. The explicit extrapolation uses the Newton polynomial, built on known values of the convection terms from the 3 previous time steps, to evaluate the convective term for the new time step, the detailed description of the extrapolation can be found in Karniadakis et al [23]. The linear diffusion terms are treated implicitly using the 3rd-order backward differencing scheme (BDF3). The implicit scheme again makes use of the Newton polynomial, but it is built on known values of velocity at 2 previous time steps and an unknown value of velocity at the future time step.

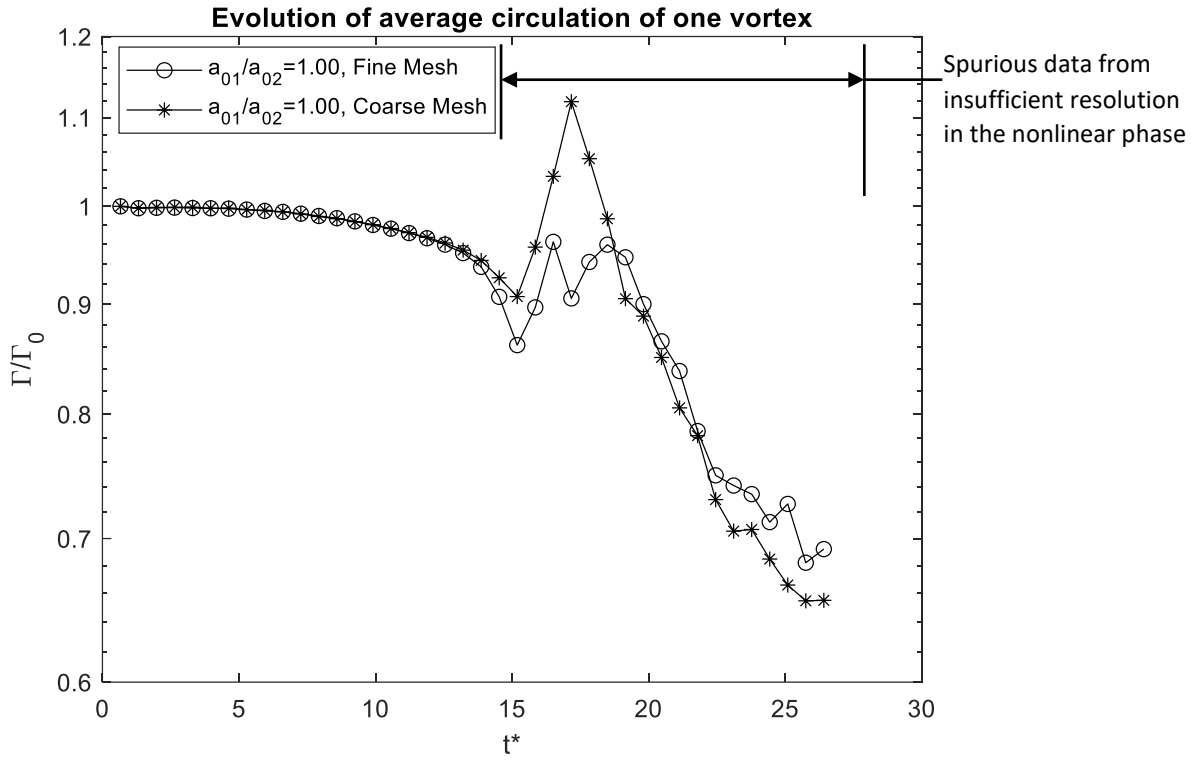

Figure II.5: Evolution of the circulation of one vortex in fine mesh, coarse mesh, showing spurious data in the nonlinear phase.

Chapter III Simulation Results

In this chapter, the basic development of the flow and instability are presented. Both qualitative and quantitative results of the simulations are provided through visualization of some of the characteristic quantities in the flow. Representative results for the symmetrical pair, weakly asymmetrical pair, and strongly asymmetrical pair are shown.

III.A Two-Dimensional Basic Behavior

Despite the three-dimensional nature of the instability, certain aspects of the vortex interaction can still be explained by two-dimensional vortex dynamics.

During the early development of the flow, the two vortices move due to their induced velocity, which follows that of two point vortices if the aspect ratio remains sufficiently small. In the simulations of symmetrical or weakly asymmetrical counter-rotating vortex pairs, it is observed that the vortices translate in a straight line downward, perpendicular to the line connecting them, with speed $W_0 = \frac{\Gamma_0}{2\pi b_0}$ as defined in Eq. II-3. The translation occurs because the circulation of the vortices remains comparable throughout the duration of the simulation, and the velocity field generated from each vortex induces a downward velocity in the other.

For the strongly asymmetrical cases, the pair is seen to travel in a straight line initially, but then starts to rotate around each other in the linear phase. This rotation is consistent with the behavior of two vortices with unequal circulation shown in [19], where the pair would rotate around one another with the angular velocity:

$$\Omega = \frac{\Gamma_1 + \Gamma_2}{2\pi b^2} \qquad \text{Eq. III-1}$$

around a point on the line connecting both vortices. The point is located from vortex 1 (respectively, vortex 2) by a distance of

$$b_1 = \frac{\Gamma_2 b}{\Gamma_1 + \Gamma_2} \quad (\text{respectively}, b_2 = \frac{\Gamma_1 b}{\Gamma_1 + \Gamma_2}) \qquad \text{Eq. III-2}$$

This behavior is attributed to a more rapid circulation decrease in one of the vortices due to the strong asymmetry, the details of which is discussed in the next chapter.

It is also discussed in [19] that the separation distances between the vortices remain constant. For comparison, the separation distances for the current simulations are evaluated. For the simulated pair of counter-rotating vortices, the centers of the vortices are taken to be at grid points with the maximum and minimum vorticity values on each z-plane. The average separation distance *b* is the average of the separation between the vortex centers on each z-plane:

$$b = \frac{1}{n_z}\sum_{k=1}^{n_z}\sqrt{\left(x_{min,k} - x_{max,k}\right)^2 + \left(y_{min,k} - y_{max,k}\right)^2} \qquad \text{Eq. III-3}$$

where $(x_{min,k}, y_{min,k})$ and $(x_{max,k}, y_{max,k})$ are respectively the points of minimum and maximum vorticity on each k^{th} z-plane. Figure III.1 illustrates the time evolution of the average separation distance between the vortex centers. Across all simulations, the separation distances stayed relatively constant in the linear phase. The small deviation from the unvarying separation distance discussed in [19] can be attributed to the fact that the simulations are performed with vortices with finite core size, as opposed to the point vortex model from [19]. However, the results do align with the unstratified counter-rotating vortex pair simulation in [16]. It is also noted that the separation distances correlate well with the vortex core size ratio between the vortices, further indicating that the initial separation distance development is largely influenced by the finite core sizes.

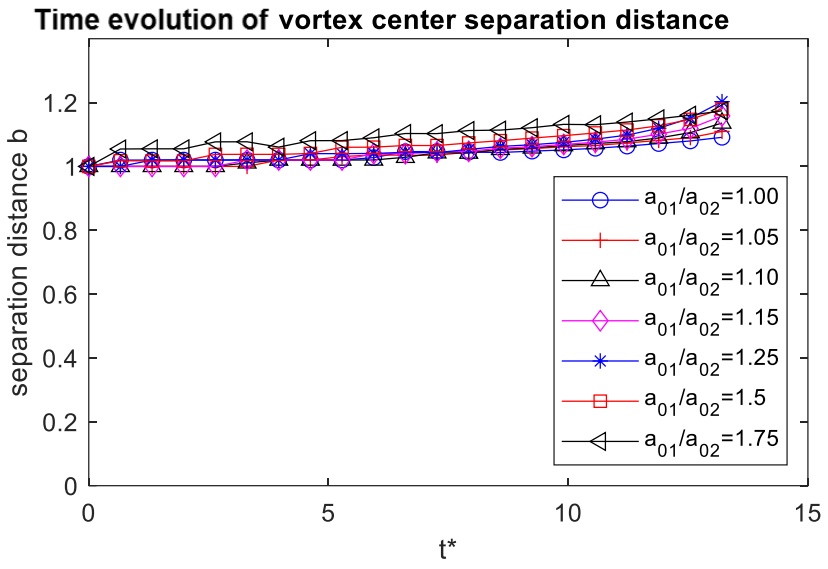

Figure III.1: Time evolution of normalized vortex center separation distance for all simulations in the linear phase.

Aside from the vortex trajectories, there are also changes to the vortex profiles due to the two-dimensional dynamics. In the transition phase, as mentioned in Section II.D.2, the superimposed Lamb-Oseen vortices from the initial condition adapt to the external strain rate induced by the other vortex, and their profiles become more elliptical rather than circular. The external strain rate, S_e, is the strain rate induced by the partner vortex on a vortex (at the location of peak vorticity) without accounting for the presence of that vortex. The elliptical profile is illustrated by the contour plot of axial vorticity magnitude on the x-y plane in Figure III.2. This behavior is consistent across all simulations; however, for the asymmetrical cases, the vorticity contours and the streamlines are more deformed for one vortex than the other.

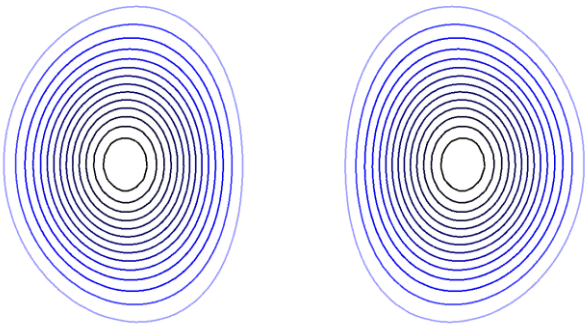

Figure III.2: Contour plot of axial vorticity showing elliptical deformation of initially axisymmetric vortices after the transition phase.

III.B Three-Dimensional Flow Development

There are several parameters that are commonly used for the visualization of vortices in numerical simulations, that of which used in this study is the Q-criterion first proposed by Hunt et al [24].

The Q-criterion, also known as the second invariant of the velocity gradient tensor, *II*, can be used to visualize regions in the flow where vorticity is higher than the rate of strain. For an incompressible flow, it is calculated by:

$$II = \frac{\|A\|^2 - \|S\|^2}{2} \qquad \text{Eq. III-4}$$

A is the rate of rotation tensor and *S* is the rate of strain tensor. To simplify comparison between the different simulations, the second invariant is nondimensionalized using the initial average enstrophy of each of the simulations, $\overline{\omega_0^2}$.

$$II^* = \frac{II}{\overline{\omega_0^2}/4} \qquad \text{Eq. III-5}$$

Figure III.4, 6, 8 show contour plots of II^* for representative simulations of vortex pairs with varying levels of asymmetry, quantified by the ratio of their initial core radii. Plots for the

cases a_{01}/a_{02} =1, a_{01}/a_{02} =1.1, a_{01}/a_{02} =1.75 illustrate the evolution of symmetrical, weakly asymmetrical, and strongly asymmetrical pairs, respectively. The various stages of the fluid flow for all simulations are summarized in Table III.1. In the transition phase, the perturbation decays due to viscous diffusion, and can be identified as the timeframe from the start of the simulation to the time that the average off-axial vorticity reaches its minimum (Figure IV.9). In the linear phase, unstable perturbations grow exponentially, and sinusoidal deformation develops on vortices; this phase occurs after the transition phase and before the nonlinear phase. In the nonlinear phase, the perturbation amplitudes become large and no longer grow exponentially; the phase can be visually identified by the formation of the secondary structures and transverse vorticity bridges (Figure III.4, 6, 8).

Table III.1. Start of transition, linear, and nonlinear phases of vortex pair evolution

	Transition Phase	Linear Phase	Nonlinear Phase
a_{01}/a_{02}= 1.00	t* ≤ 4.62	4.62 < t* ≤ 15.19	15.19 < t*
a_{01}/a_{02}= 1.05	t* ≤ 4.62	4.62 < t* ≤ 14.53	14.53 < t*
a_{01}/a_{02}= 1.10	t* ≤ 4.62	4.62 < t* ≤ 13.86	13.86 < t*
a_{01}/a_{02}= 1.15	t* ≤ 4.62	4.62 < t* ≤ 13.86	13.86 < t*
a_{01}/a_{02}= 1.25	t* ≤ 4.62	4.62 < t* ≤ 13.86	13.86 < t*
a_{01}/a_{02}= 1.50	t* ≤ 4.62	4.62 < t* ≤ 13.86	13.86 < t*
a_{01}/a_{02}= 1.75	t* ≤ 4.62	4.62 < t* ≤ 13.21	13.21 < t*

III.B.1 Symmetrical Pair

The flow behavior in a symmetrical vortex pair with equal circulation magnitude, core radii, and peak vorticities have been extensively studied in literature. A simulation is run with comparable conditions and parameters as the asymmetrical cases in this study to provide a baseline for comparison of the different phases in the simulation.

During the linear growth phase, the random perturbations develop into the distinct sinusoidal deformation of the elliptical instability, as seen in Figure III.4 t*=10.57-14.53. The antisymmetric modes of the elliptical instabilities can be seen to grow equally on both vortices,

which is further illustrated in the comparable levels of core deformation and displacement in each of the vortices in Figure III.3. Once the deformation reaches large amplitude, nonlinear phase begins, each displaced vortex core draws in vorticity from the other vortex, causing vorticity bridges to form between the pair (Figure III.4, t*= 15.85). These transverse vorticity bridges further develop and bring together vorticity of opposite sign, resulting in the decay of the primary vortices (Figure III.4, t*= 17.17).

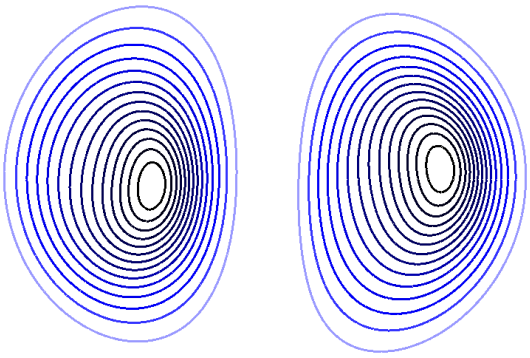

Figure III.3: Symmetrical pair (a_{01}/a_{02}= 1.0) axial vorticity magnitude contour in the linear growth phase (t*=11.89)

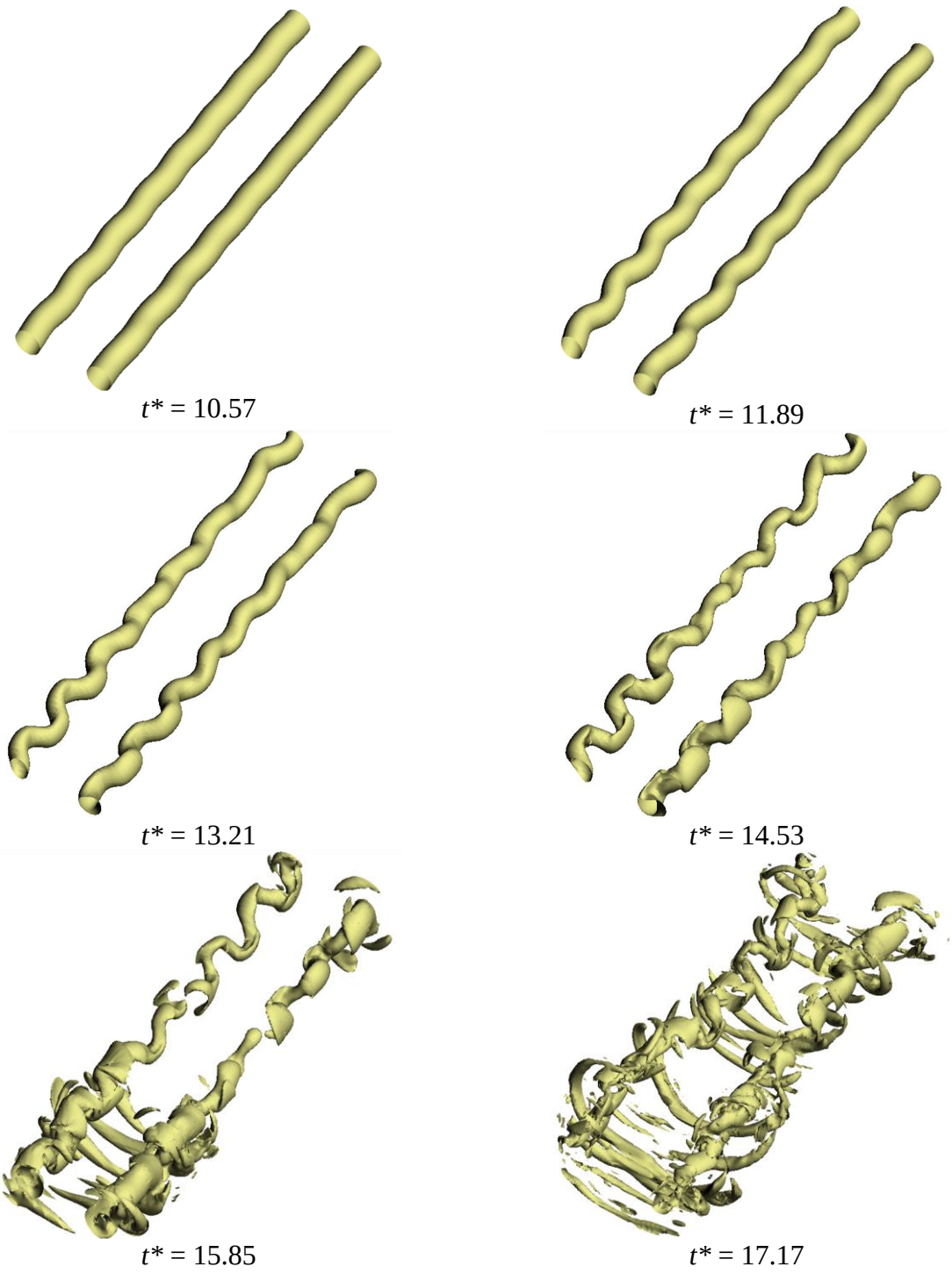

Figure III.4: Flow visualization of II^*=60 for a_{01}/a_{02}= 1.0 at t^* = 10.57, 11.89, 13.21, 14.53, 15.85, 17.17.

III.B.2 Asymmetrical Pair

In general, for a pair of unequal vortices, the external strain rate exerted by each vortex on the other may differ in strength. The stronger vortex, which in existing literature and research is often the one with the larger initial circulation, strains the weaker vortex more strongly, as the external strain rate S_e felt by one vortex scales directly with the circulation of the other vortex.

$$S_{e1} = \frac{\Gamma_2}{2\pi b^2}, \qquad S_{e2} = \frac{\Gamma_1}{2\pi b^2} \qquad \text{Eq. III-6}$$

This causes the instabilities to grow more rapidly on the weaker vortex while allowing the stronger vortex to be less affected by the weaker strain field. Depending on the level of asymmetry, the weaker vortex may shed too much vorticity and be destroyed before the stronger vortex experiences any significant deformation.

In the current study, the asymmetrical vortex pairs have the same initial circulation and same S_e but different core sizes and peak vorticities. The identification of the weaker and stronger vortices in the simulation cannot rely solely on their circulations. However, the perturbations have been observed to grow more rapidly on the vortex with the larger core size and lower peak vorticity in the pair for all simulations. This vortex is then deemed as the weaker vortex. Later in Chapter 4, the evaluation of the *relative strain* at the vortex centers quantitatively supports this identification of the weaker and stronger vortex.

Weakly Asymmetrical Pair

In the weakly asymmetrical pair, while the elliptical deformation of vortex 1 is greater (Figure III.6, t*=10.57-13.21), the stronger vortex is still significantly affected by the weaker vortex's strain field; it's seen in Figure III.5 that the core of the stronger vortex on the right is displaced, albeit by a smaller amount than the core of the weaker vortex on the left.

In the linear regime, one can see that a longer wavelength perturbation dominates as the most unstable mode compared to the symmetrical pair simulation (Figure III.6, t*=14.53). This is consistent with the known results that elliptical instability wavelength scales with core size of the vortices, since the altered vortex in the asymmetrical cases have larger core sizes. There is also sufficient vortex interaction for the formation of secondary structures from each of the vortices' transverse vorticity component (Figure III.6, t*=14.53-15.85). Eventually, it leads to the complete destruction of the weaker vortex and a partial destruction of the stronger vortex, as demonstrated by the remnants of the primary vortex structure in Figure III.6, t*=17.17.

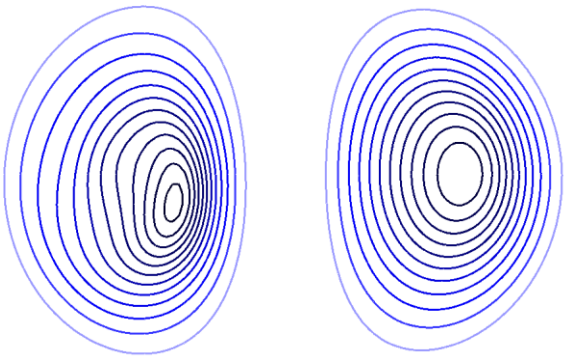

Figure III.5: Weakly asymmetrical pair (a_{01}/a_{02}= 1.1) axial vorticity magnitude contour in the linear growth phase (t*=11.89)

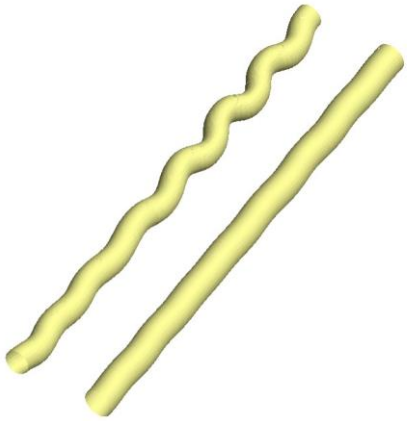

t^* = 10.57

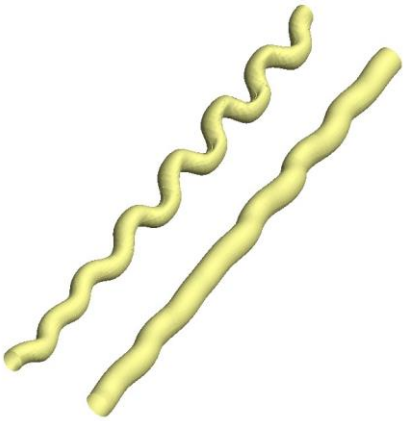

t^* = 11.89

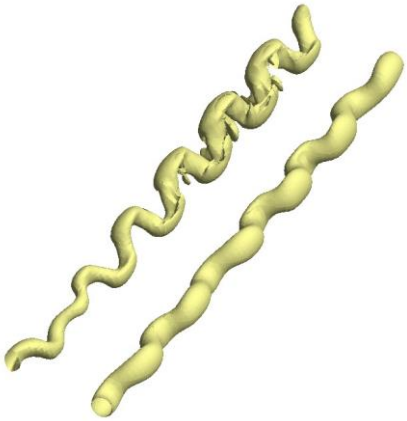

t^* = 13.21

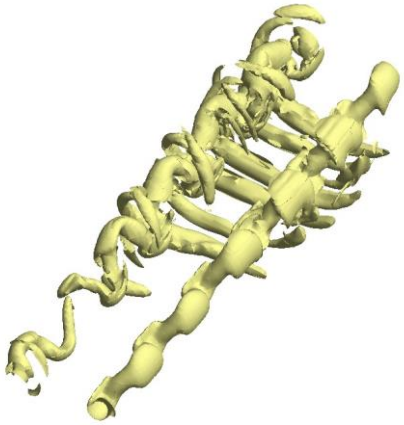

t^* = 14.53

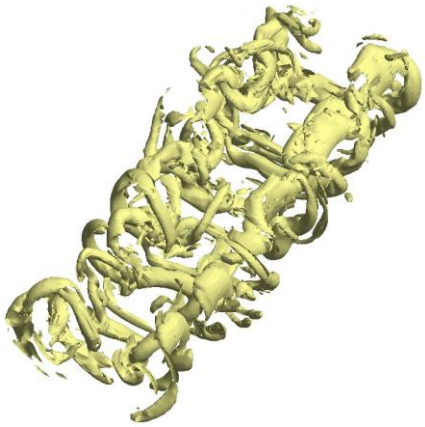

t^* = 15.85

t^* = 17.17

Figure III.6: Flow visualization of II^*=100 for a_{01}/a_{02}= 1.1 at t^* = 10.57, 11.89, 13.21, 14.53, 15.85, 17.17.

Strongly Asymmetrical Pair

With increased asymmetry, the stronger vortex is only minimally affected by the weaker vortex's strain field, where no core displacement and very little perturbation growth is observed in the linear phase (Figure III.7, Figure III.8 t*=10.57-12.56). The most unstable mode has an even longer wavelength than in the weakly asymmetrical cases (Figure III.8 t*=12.56-14.53). In the nonlinear regime, the weaker vortex's transverse vorticity forms secondary vorticity bridges which wrap around the stronger vortex (Figure III.8 t*=16.51-18.49). The secondary structures then interact with the primary structure of the stronger vortex which leads to partial destruction.

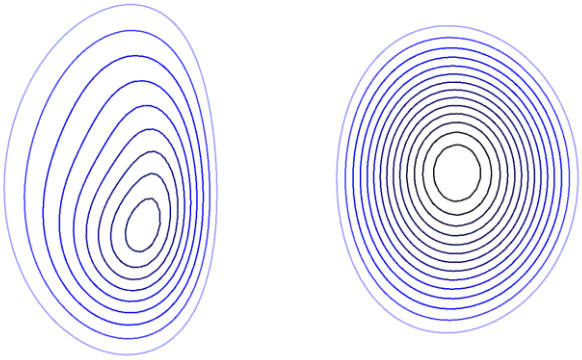

Figure III.7: Strongly asymmetrical pair (a_{01}/a_{02}= 1.75) axial vorticity magnitude contour in the linear growth phase (t*=12.55).

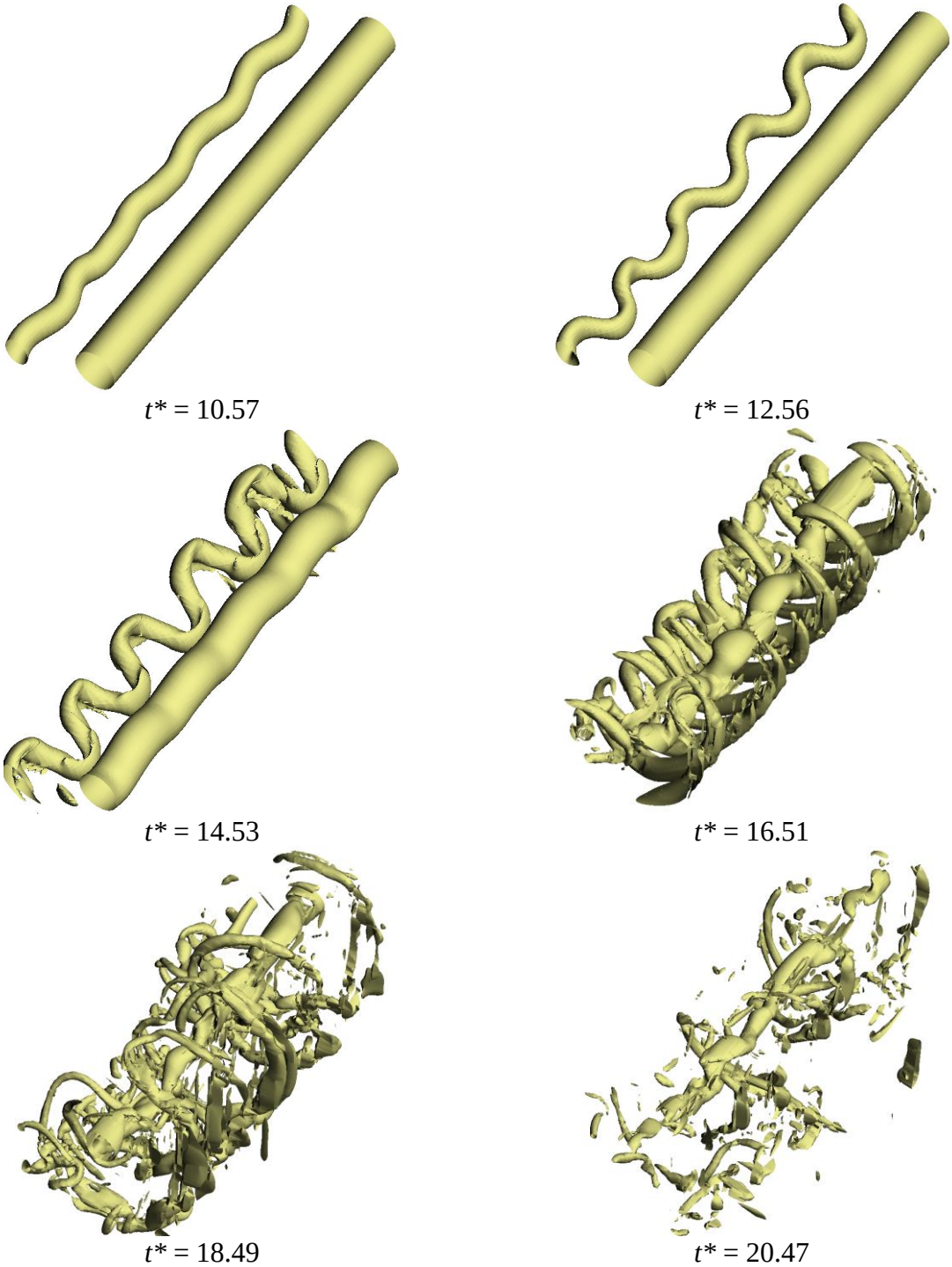

Figure III.8: Flow visualization of II^*=60 for a_{01}/a_{02}= 1.75 at t^* = 10.57, 12.56, 14.53, 16.51, 18.49, 20.47.

Chapter IV Analysis of Elliptical Instability

In this chapter, the development of the flow and the elliptical instability in the linear phase is examined in more detail. In Section IV.A, the distinct geometry of the elliptical instability as seen in the simulations is described qualitatively and quantitatively. In Section IV.B, global measurements that pertain to the behavior observed in Chapter 3 are analyzed, spectral analysis is done on the simulation data to investigate the correlation between the unstable perturbation wavelengths, their growth rates, and the asymmetry in the vortex pair. In Section IV.C, the growth rates of the instability are compared against the theoretical prediction in the existing literature.

IV.A Geometry and Phase Relations

One of the main indicators of elliptical instability is its anti-symmetric modes that grow on each of the two vortices as mentioned in Section I.B.1. The perturbed vortex centers develop into sinusoidal waveforms when the evolution is well into the linear phase. For the current study, the vortex centers are taken as the grid points with the highest and lowest vorticities on each z-plane for a counter-rotating pair that is symmetrical (Figure IV.1), weakly asymmetrical (Figure IV.2), and strongly asymmetrical (Figure IV.3). The figures for the symmetrical case (Figure IV.1) are overlaid with the II*=95 contour surface for validation against vortex visualization.

The symmetrical case compares well to the experimental results in [1] and the DNS results in [10], where the top view shows the waveforms on the vortices to be in phase while the side view shows the waveforms being out of phase. The end view shows that the plane on which the perturbations amplify is less than 45 degrees from the horizontal, this again agrees with DNS results from [10] and [16] for the later stages of the linear phase. For the weakly asymmetrical case, the same phase relation is still present, though it is somewhat complicated by the competing perturbation modes in the vortex pair at this timestep. For the strongly asymmetrical vortex pair,

despite the small amplitude in the perturbation waveform on the stronger vortex, the anti-symmetric phase relation can still be discerned in the side view of Figure IV.3. The weaker vortex's rotation around the stronger vortex as discussed in Section III.A is also captured in the end view of Figure IV.3.

By taking a section cut through the centers of both vortices, it can be seen that the internal structure of the transverse vorticity for the same three cases (Figure IV.4) compare well with the visualization in [9] and [10]. The transverse vorticity grows predominantly on the weaker vortex; this is expected since the fluid that circulate around the sinusoidally displaced vortex cores generates vorticity in the off-axial direction. Hence, the larger core displacement in the weaker vortex leads to larger magnitude of transverse vorticity.

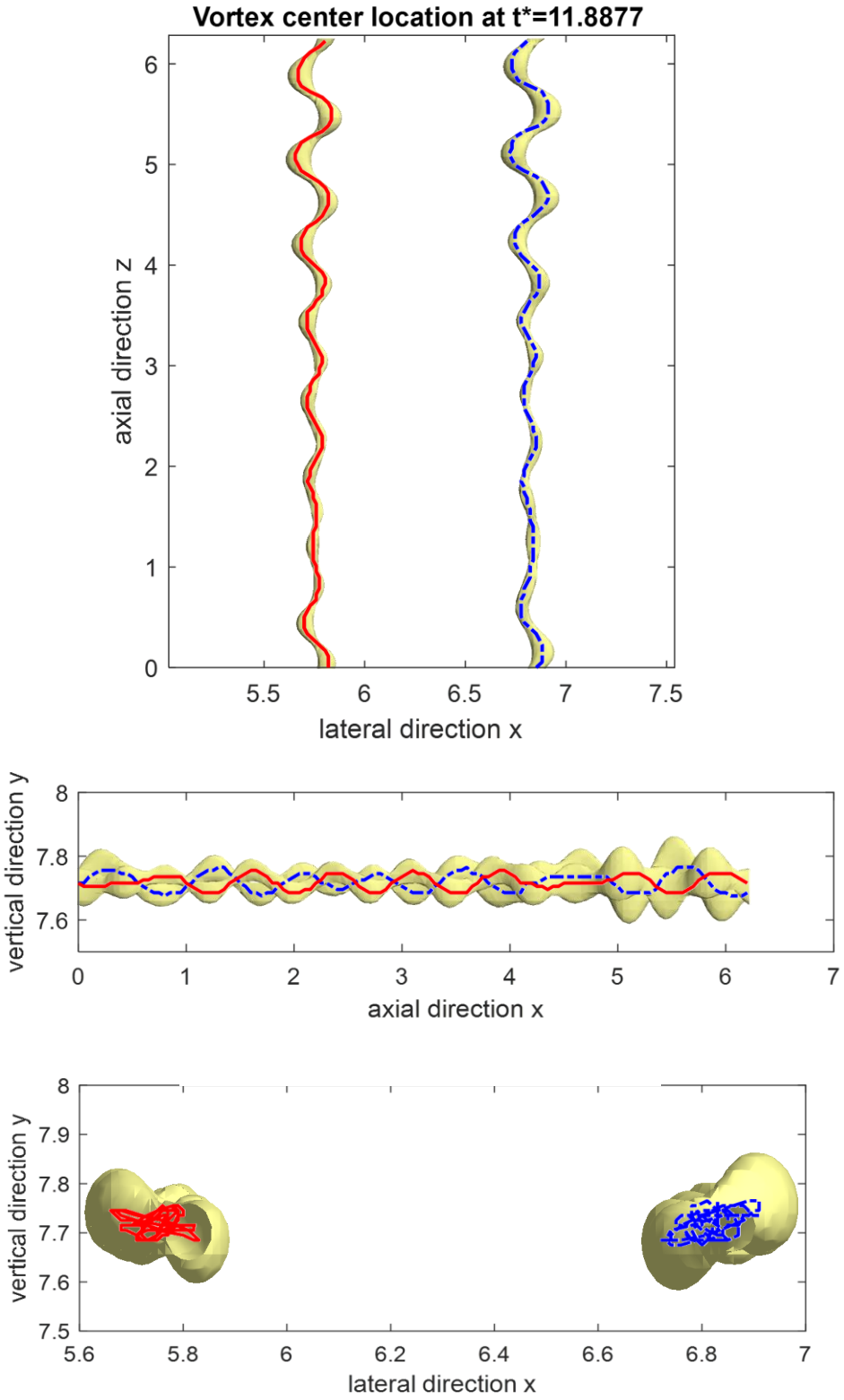

Figure IV.1: Top, side, and end view of symmetrical pair (a_{01}/a_{02}= 1.00) vortex center location overlaid with II*=95 contour surface in the linear growth phase (t*=11.89).

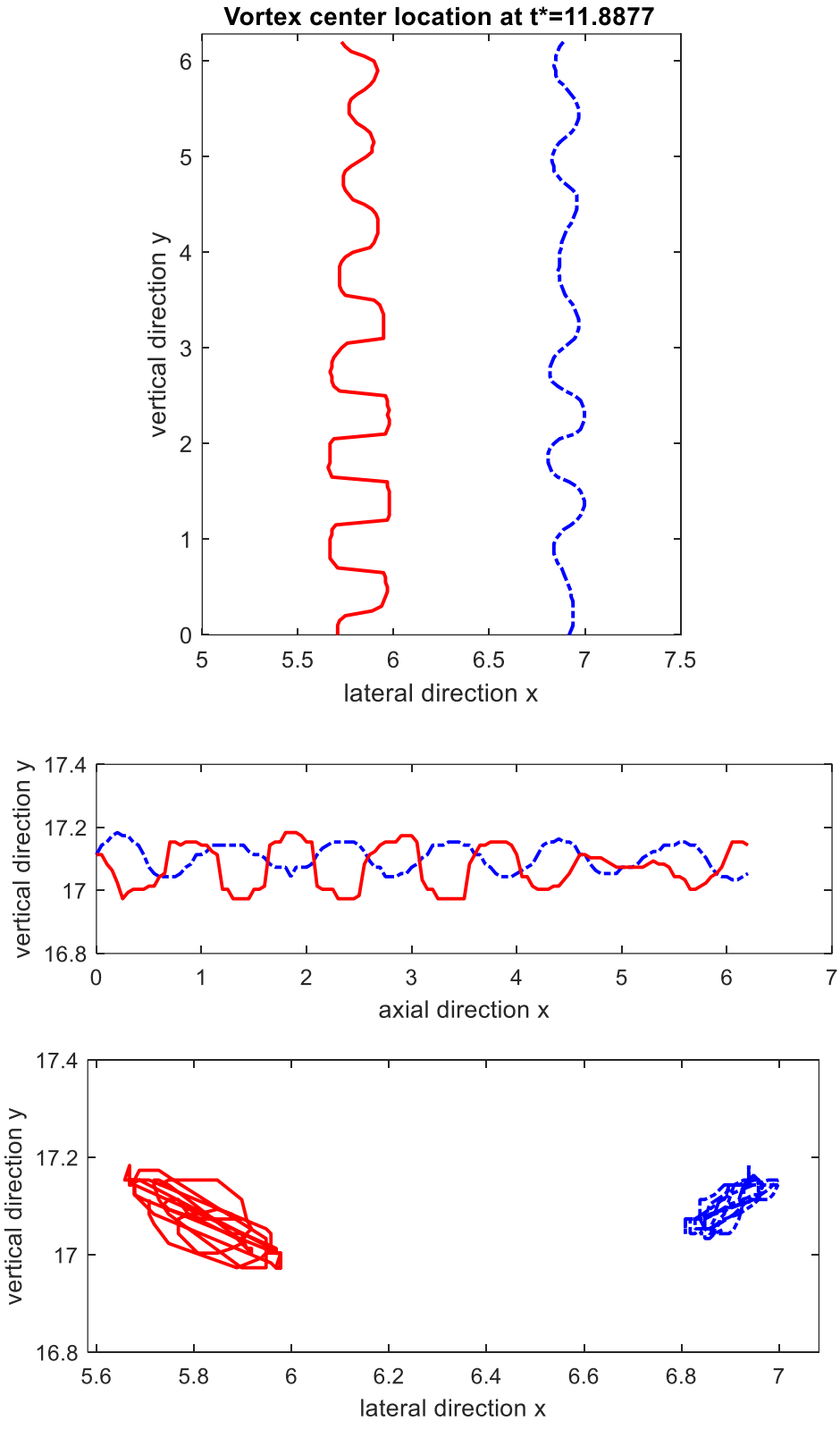

Figure IV.2: Top, side, and end view of weakly asymmetrical pair (a_{01}/a_{02}= 1.10) vortex center location in the linear growth phase (t*=11.89).

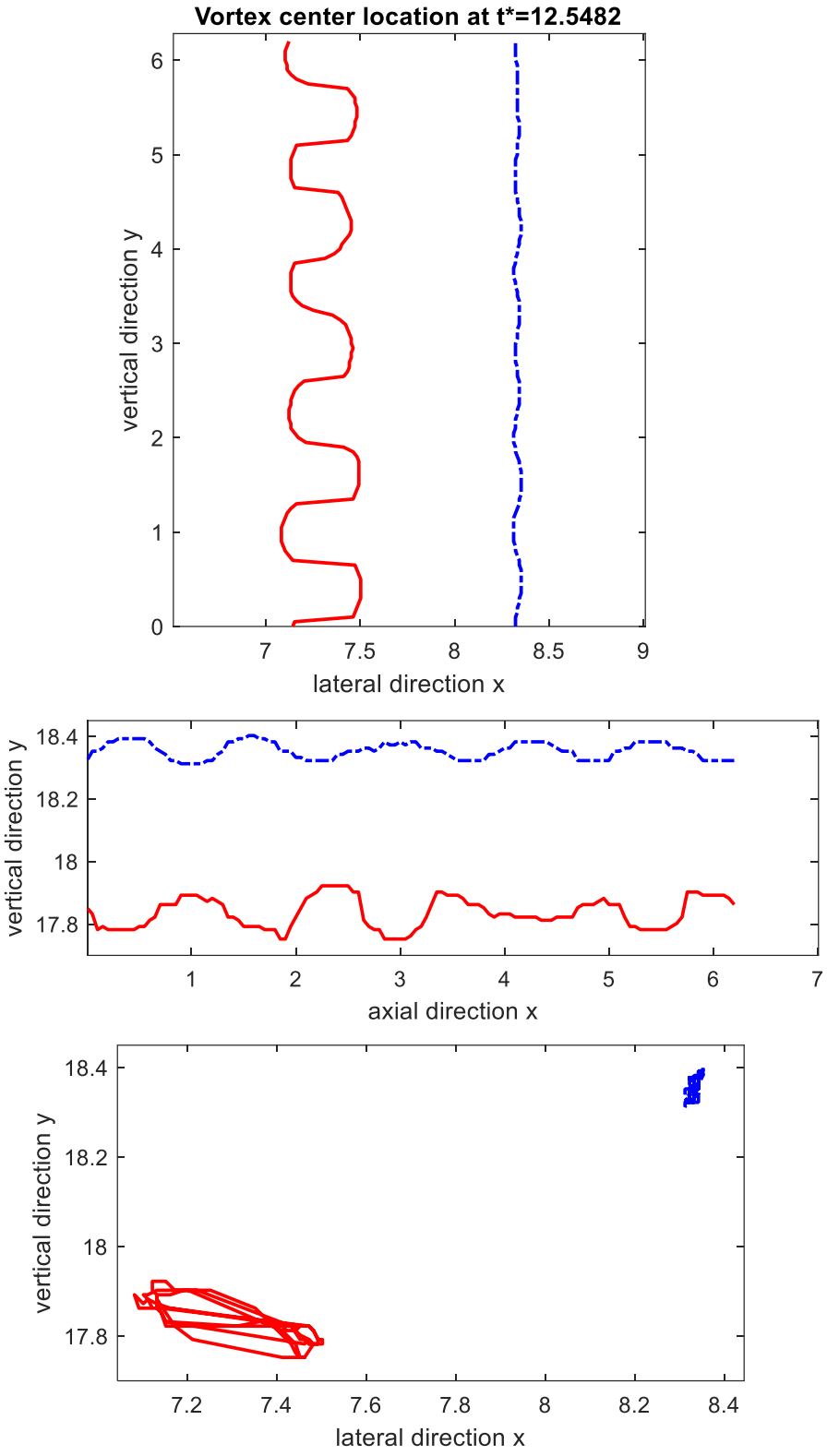

Figure IV.3: Top, side, and end view of strongly asymmetrical pair (a_{01}/a_{02}= 1.75) vortex center location in the linear growth phase (t*=12.55).

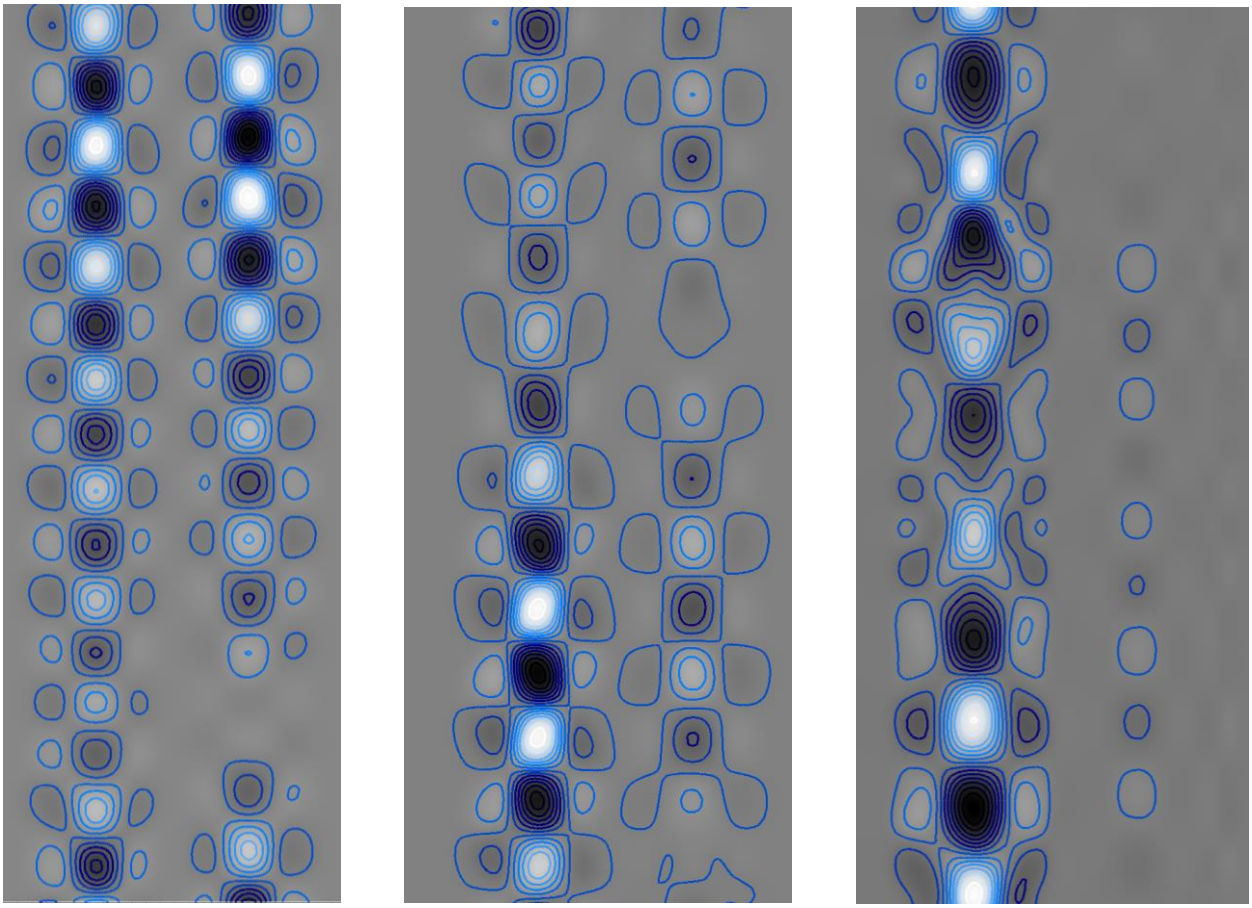

Figure IV.4: Transverse vorticity radial structure viewed on sectional cut plane through both vortex centers for a_{01}/a_{02}= 1.00 at t^* =11.23 (left), a_{01}/a_{02}= 1.10 at t^* =11.23 (middle), a_{01}/a_{02}= 1.75 at t^* =10.56 (right).

IV.B Quantitative Analysis

In this section, global measures in the flow and their pertinence to the linear phase flow development are evaluated and discussed, spectral analysis is performed, and the effects of core size and peak vorticity variations on the instability growth rate are examined.

IV.B.1 Global Measures of the Linear Phase Flow Development

Circulation

Circulation is an obvious global quantity to track for a flow with two initially parallel, counter-rotating vortices. For a three-dimensional flow with two equal-strength vortices, the circulation for one of the vortices is evaluated as

$$\Gamma = \frac{1}{L_z}\int_{L_z}\left(\int_{L_x/2}\int_{L_y}\omega_x(x,y,z)\,dy\,dx\right)dz \qquad \text{Eq. IV-1}$$

The vorticity is integrated over half of the domain in the transverse direction since for an equal-strength pair, the vortices propagate vertically downwards, so the vorticity associated with each of the vortices remain in their respective half of the domain. However, in the current study, this method of evaluating the circulation is not always viable; for the strongly asymmetrical cases, the weaker vortex rotates around the stronger vortex in the linear phase, entering the opposite half of the domain. However, because the counter-rotating vortices have vorticity of opposite sign, the circulation of each of the vortices can be evaluated as follows

$$\Gamma_1 = \frac{1}{n_z}\sum_{i=1}^{n_z}\left(\sum_{j=1}^{n_y}\sum_{k=1}^{n_x}\omega_{z1}(x_i,y_j,z_k)\,\Delta x\Delta y\right) \qquad \text{Eq. IV-2}$$

$$\Gamma_2 = \frac{1}{n_z}\sum_{i=1}^{n_z}\left(\sum_{j=1}^{n_y}\sum_{k=1}^{n_x}\omega_{z2}(x_i,y_j,z_k)\,\Delta x\Delta y\right) \qquad \text{Eq. IV-3}$$

where ω_{z1} is the negative-signed vorticity value associated with the clockwise vortex 1, and ω_{z2} is the positive-signed vorticity associated with the counterclockwise vortex 2. Furthermore, since the simulations are initialized with a white noise perturbation field in addition to the two-vortex flow, a conditional circulation $<\Gamma>$ is used to better represent the circulation associated with the two primary vortices. Specifically, $<\Gamma>$ is evaluated by only considering vorticity at least 2.5%

of the peak vorticity of each of the vortices ($\omega_{z1} < 0.025\ \omega_{z,min}$ and $\omega_{z2} > 0.025\ \omega_{z,max}$) so that perturbations at the far fields do not significantly impact the evaluation.

The conditional circulation for vortices 1 and 2 is shown in Figure IV.5 and Figure IV.6, respectively. As mentioned in Section III.A, vortex 1 (weaker vortex) sees a larger decrease in its circulation as the pair becomes more asymmetrical, resulting in the rotation of one vortex around another. Vortex 2 (stronger vortex) experiences an overall smaller decrease in circulation towards the end of the linear phase for the strongly asymmetrical cases. However, vortex 2 does not necessarily see a smaller decrease in circulation in the weakly asymmetrical cases as one would expect.

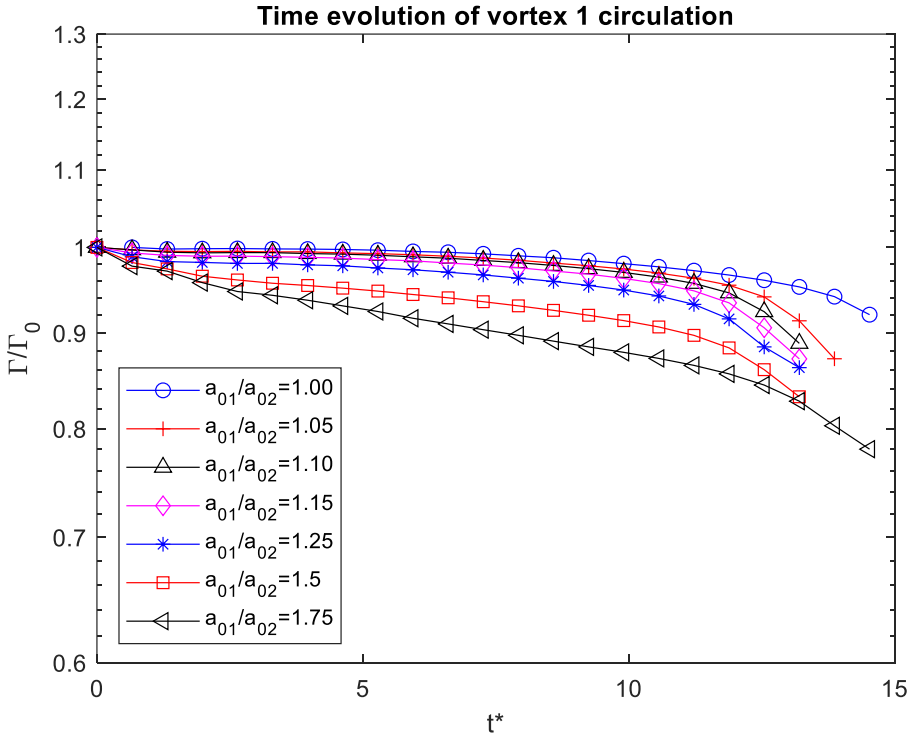

Figure IV.5 Conditional circulation < Γ > of vortex 1 for all simulations.

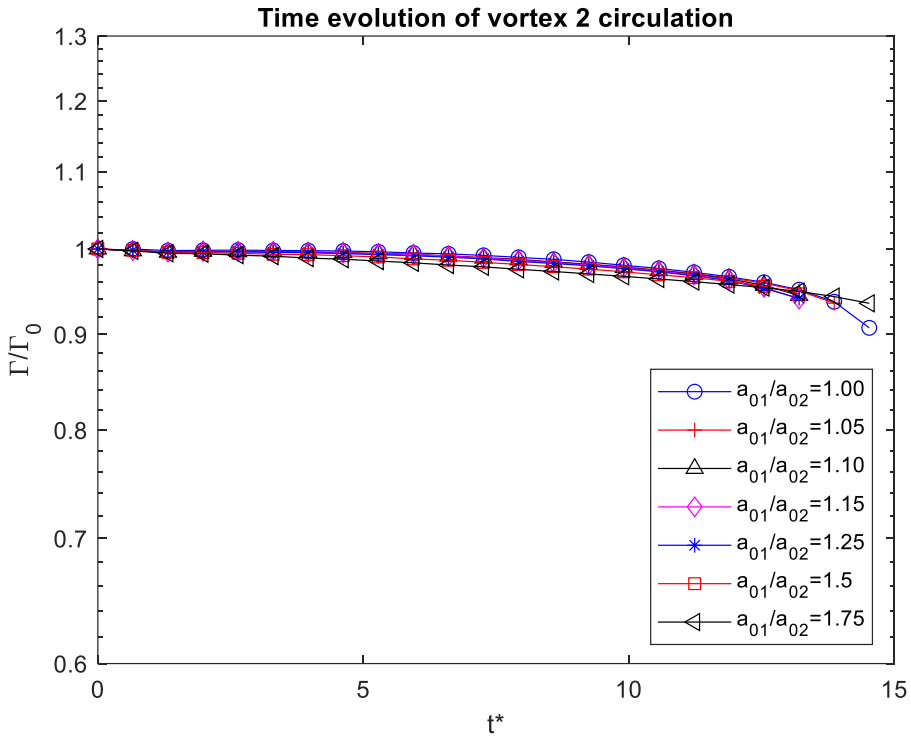

Figure IV.6: Conditional circulation < Γ > of vortex 2 for all simulations

The time evolution of circulation on the vortices can be explained by the relative strain $\left|\frac{S_{i1}}{\omega_{01}}\right|, \left|\frac{S_{i2}}{\omega_{02}}\right|$ at the vortex centers in Figure IV.7 and Figure IV.8. Here, S_{i1} and S_{i2} are the internal strain rate magnitudes measured on vortices 1 and 2 centers, respectively. In contrast with the external strain rate, S_e, the internal strain rate is the actual strain rate that occurs due to the interaction between the two vortices. On vortex 1, the relative strain increases with increased asymmetry within the pair, which can be attributed to its lower vorticity magnitude being less apt at counteracting the external strain rate from vortex 2 and the internal strain rate enhanced by its own deformation. In the strongly asymmetrical cases, vortex 1 then sheds more vorticity at a faster rate, resulting in significant reduction in circulation. This circulation reduction in vortex 1 then leads to a smaller strain rate and relative strain acting on vortex 2. The larger relative strain associated with lower peak vorticity quantitatively supports the identification of vortex 1 as the weaker vortex in Section III.B.2.

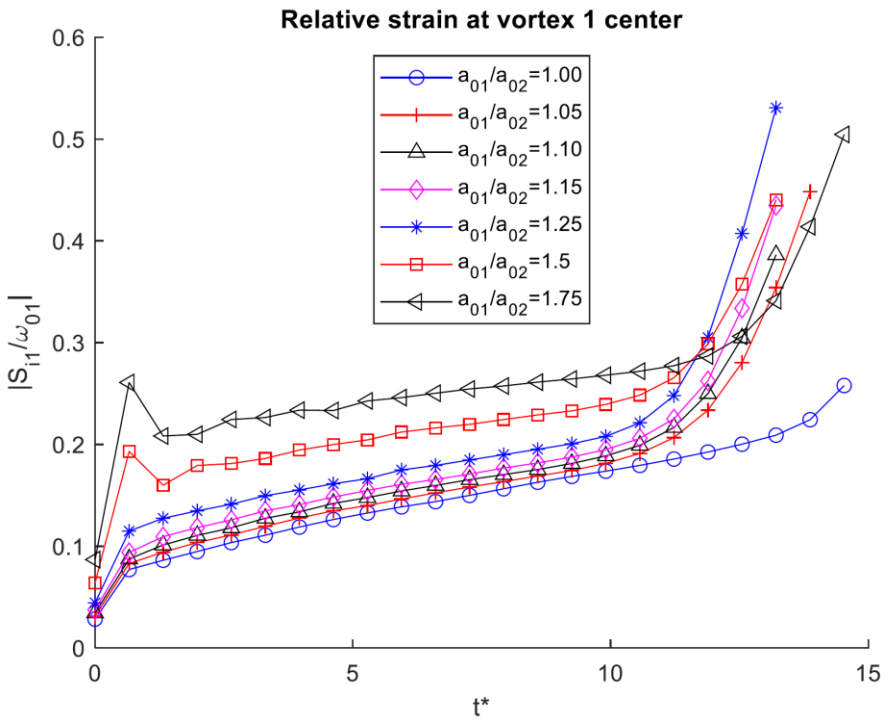

Figure IV.7: Relative strain at vortex 1 center for all simulations.

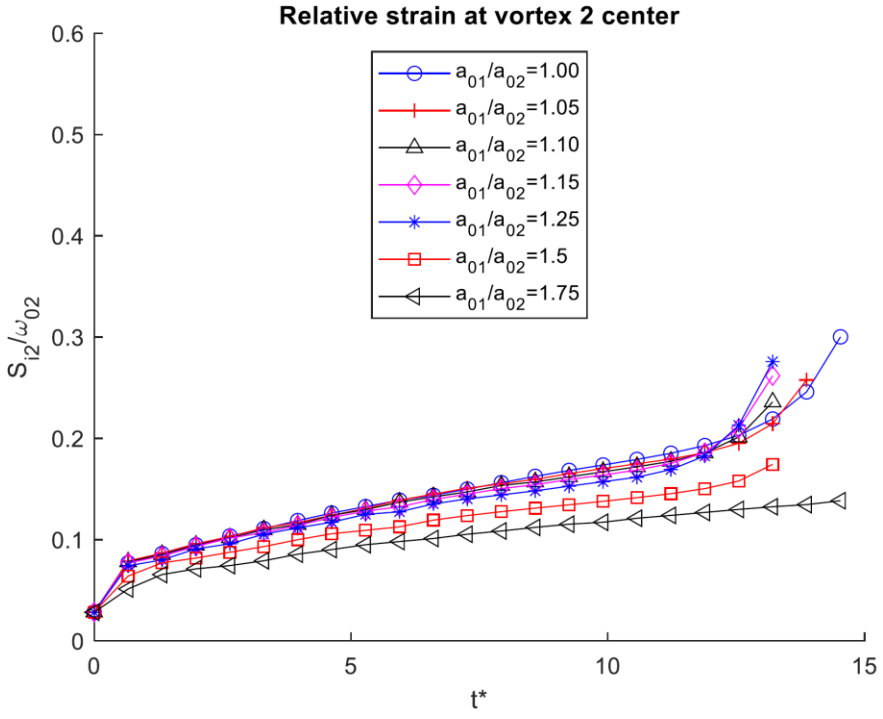

Figure IV.8: Relative strain at vortex 2 center for all simulations.

Global Average of Transverse Vorticity

The development of the transverse vorticity can also be used to characterize the growth of the elliptical instabilities in the flow. Per Figure III.4, as the instabilities grow, the initially parallel vortices are deformed sinusoidally. Their vorticity, which was predominantly in the axial direction, are reoriented following the waveform of the growing perturbation mode to develop larger transverse and vertical components. Since the secondary vorticity structures in the nonlinear phase have been mainly developing in the transverse direction due to the relative positioning of the primary vortex pair, and that the transverse and vertical components of vorticity have been observed to show similar evolutions in Laporte & Corjon [10], only the transverse component of the vorticity, ω_x, is considered here. Proposed by [10], the global average of ω_x can be evaluated on a continuous domain by

$$\Gamma_x = \frac{1}{L_x}\int_{L_x}\left(\int_{L_y}\int_{L_z}|\omega_x(x,y,z)|\,dy\,dz\right)dx \qquad \text{Eq. IV-4}$$

The discrete form of Eq. IV-4 is used to evaluate the quantity for the current study

$$\Gamma_x = \frac{1}{n_x}\sum_{i=1}^{n_x}\left(\sum_{j=1}^{n_y}\sum_{k=1}^{n_z}\left|\omega_x(x_i,y_j,z_k)\right|\Delta y\Delta z\right) \qquad \text{Eq. IV-5}$$

To compare the evolution of the global average of ω_x across different simulations, the quantity is then normalized using the global average of the initial axial vorticity magnitude, Γ_{0z}.

$$\Gamma_{0z} = \frac{1}{n_z}\sum_{k=1}^{n_z}\left(\sum_{j=1}^{n_y}\sum_{i=1}^{n_x}\left|\omega_z(x_i,y_j,z_k,t*=0)\right|\Delta y\Delta x\right) \qquad \text{Eq. IV-6}$$

Again, a conditional global average of the initial vorticity magnitude $<\Gamma_z>$ is used to better represent the axial vorticity associated with the 2 primary vortices. The conditional average is evaluated by only taking into account vorticity at least 2.5% of the peak vorticity of each of the

vortices ($\omega_{z,0,} < 0.025\ \omega_{z,0,1,min}$ or $\omega_{z,0} > 0.025\ \omega_{z,0,2,max}$) on the right hand side of Eq. IV-6 so that the initial white noise is excluded from this evaluation.

The behavior of the global average transverse vorticity is shown in Figure IV.9 for all simulations. The transverse vorticity from the initial white noise decreases during the transition phase through viscous diffusion as the two vortices adapt to each other's strain field. Once the vortices have elliptical streamlines at the end of the transition phase, the unstable modes from the perturbation are amplified by the strain field, the parallel vortices are deformed into sinusoidal waves, and the transverse vorticity grow exponentially in the linear phase.

Based on Figure IV.9, linear phase growth rate of the transverse vorticity is the highest for the case of a_{01}/a_{02}= 1.25 in this study. Specifically, the growth rate for this global measure seems to increase as the asymmetry between the vortices increase from a_{01}/a_{02}= 1.00 to a_{01}/a_{02}= 1.25 but decreases again as the asymmetry increases further.

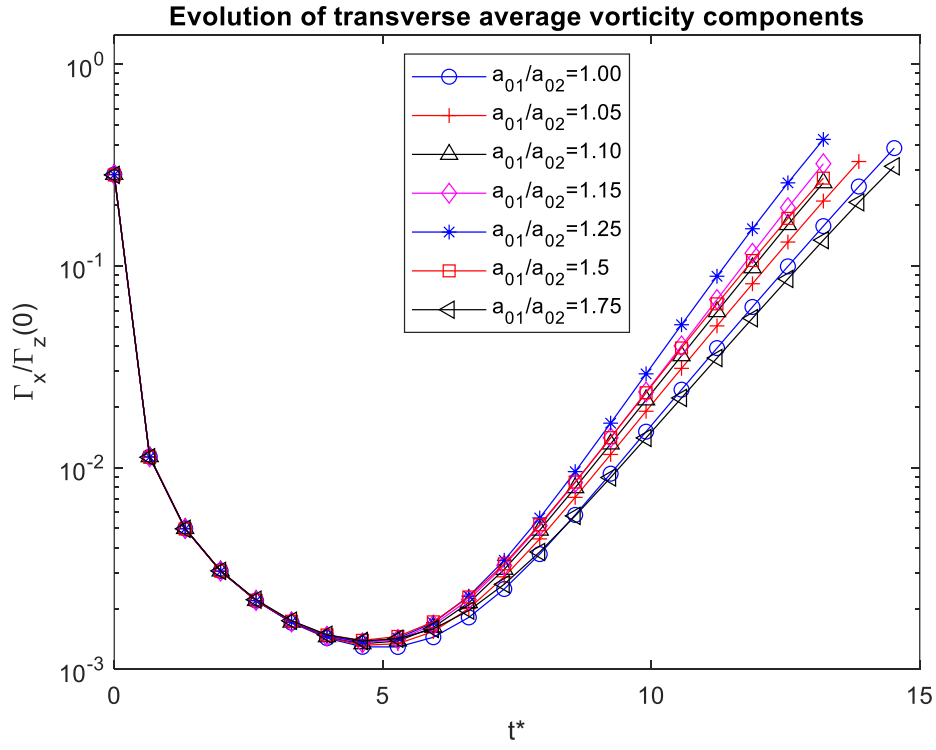

Figure IV.9: Global average of transverse vorticity for all simulations

IV.B.2 Spectral Analysis

To quantitatively assess the growth of the instability and its most unstable mode, the kinetic energy for each axial mode, $\hat{E}_k$, is evaluated as follows. The one-dimensional discrete Fourier transform is performed in the axial direction at each grid point on each of the velocity components $u_i(x, y, z, t)$, where $i = x, y, z$, to obtain $\hat{u}_i(x, y, k, t)$, which is the velocity components as a function of perturbation wavenumber k. The kinetic energy spectrum $\hat{E}_k(k, t)$ is then calculated by averaging $\hat{u}_i\hat{u}_i = \hat{u}_x\hat{u}_x + \hat{u}_y\hat{u}_y + \hat{u}_z\hat{u}_z$ in the x-y plane.

$$E_k(k, t) = \frac{1}{L_x L_y} \sum_{m=1}^{n_y} \sum_{l=1}^{n_x} \sum_{i} \hat{u}_{i,l,m}\hat{u}_{i,l,m}\, \Delta x \Delta y \qquad \text{Eq. IV-7}$$

Since the two-dimensional base flow corresponds to $k = 0$, only $E_k(k \geq 1, t)$ is examined to gauge the evolution of the perturbation kinetic energy. The wavenumber is also non-dimensionalized using the initial core size of the weaker vortex, $k^* = ka_{01}$, for easier comparison across simulations where the weaker vortex core sizes vary.

Figure IV.10 shows the perturbation kinetic energy spectrum for the symmetrical case. The perturbation energy decreases during the initial transition phase for all wavenumbers due to the two-dimensional viscous diffusion. Then as the flow goes into the linear phase, the perturbation energy associated with the unstable Kelvin modes that resonate with the strain field begin to increase. For the symmetrical case, the most unstable mode, or one with the highest perturbation kinetic energy in Figure IV.10, has the non-dimensional wavenumber of $k^*_{max} = 1.4 \pm 0.2$. This is equivalent to the dimensional wavenumber of $k = 7$, and it corresponds to the number of waves in the axial domain (of size 2π) as seen in Figure III.4 and Figure IV.1. This compares well with the most unstable wavenumber of $k^*_z = 1.5$, which corresponds to $k^*_{max} = 1.34$ reported by

Laporte and Corjon in their DNS study [10], and $\frac{\lambda}{b_0} = 0.77$ ($k^*_{max} = 1.6$) in [1]. The perturbation kinetic energy spectrum is shown for a weakly asymmetrical case and a strongly asymmetrical case in Figure IV.11 and Figure IV.12, respectively. The behavior observed for these cases are qualitatively comparable to the symmetrical case, however, it can be observed that the most unstable mode and its growth rate is different from those of the symmetrical case.

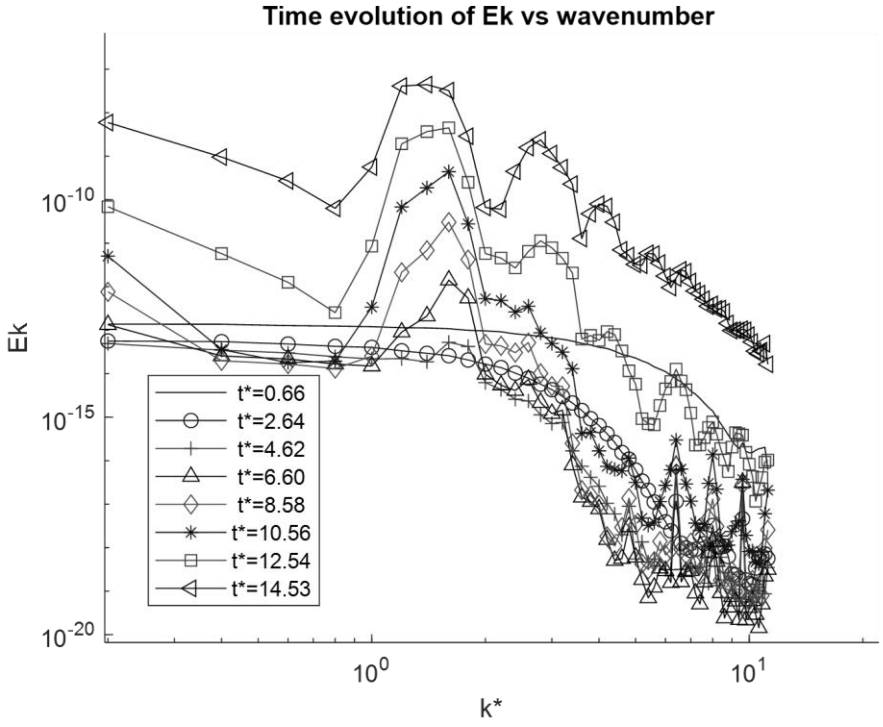

Figure IV.10: Perturbation Energy vs non-dimensional wavenumber for the symmetrical case (a_{01}/a_{02}= 1.00).

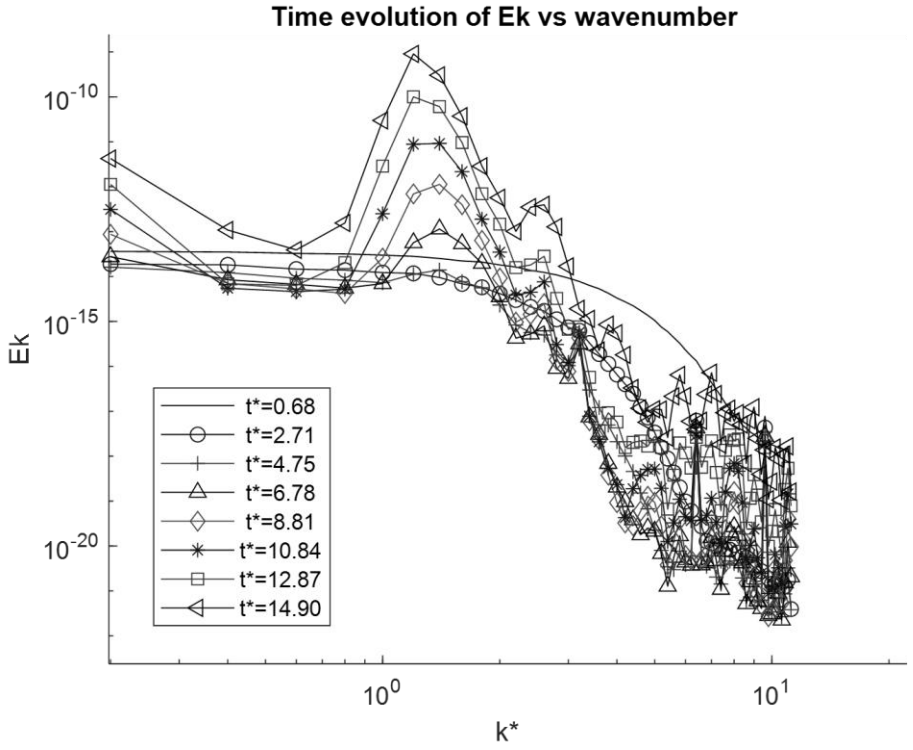

Figure IV.11: Perturbation Energy vs non-dimensional wavenumber for the weakly asymmetrical case (a_{01}/a_{02}= 1.10).

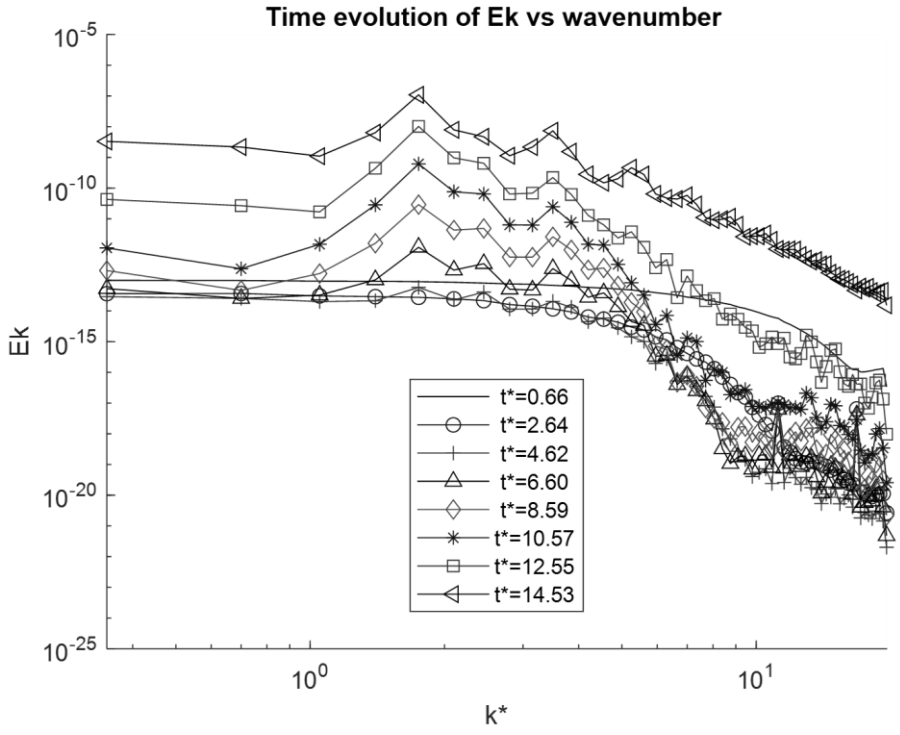

Figure IV.12: Perturbation Energy vs non-dimensional wavenumber for the strongly asymmetrical case (a_{01}/a_{02}= 1.75).

The time evolution of the perturbation kinetic energy of the most unstable modes is shown in Figure IV.13 for all simulations. The slope of the linear section of the figure is indicative of the non-dimensional growth rate of the instability for each case, which can be evaluated by

$$\sigma^* = \frac{1}{2}\frac{d(\ln E_k(k_{max}, t))}{dt^*} \qquad \text{Eq. IV-8}$$

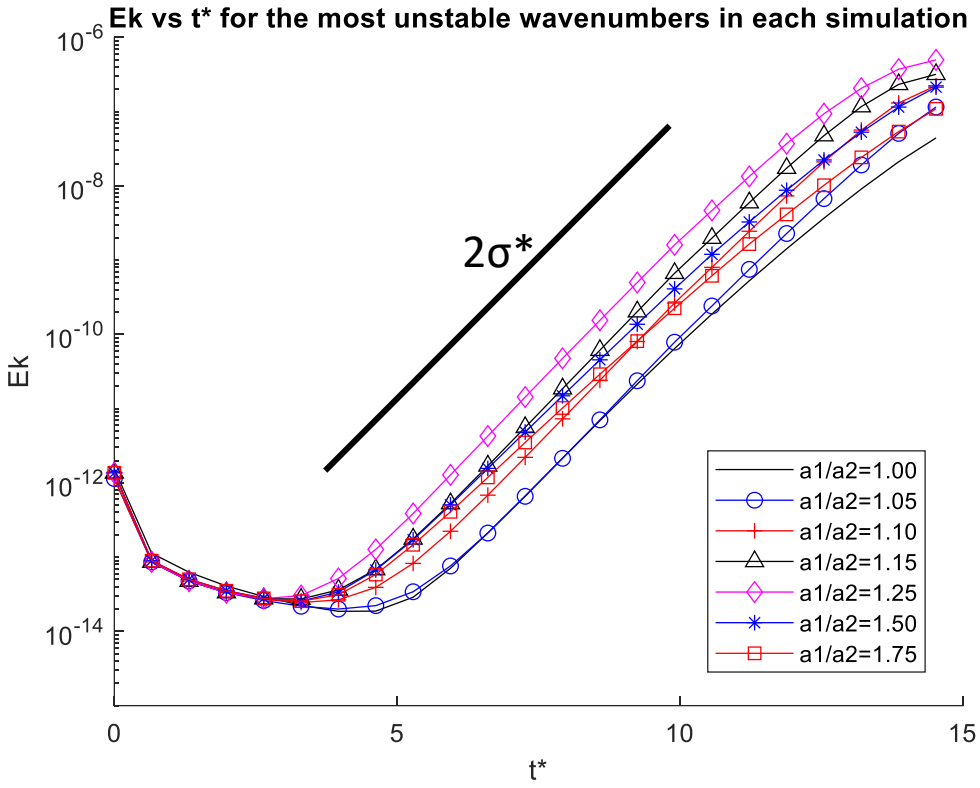

Figure IV.13: Time development for the perturbation kinetic energy for the most unstable modes in each simulation.

For the symmetrical case, the non-dimensional growth rate $\sigma^* = \frac{\sigma}{\Gamma_0/2\pi b^2} = 0.866$ for the most unstable mode compares well with the non-dimensional growth rate $\sigma^* = 0.95 \pm 0.3$ reported in [10] and $\sigma^* = 0.94 \pm 0.12$ measured in [9]. The growth rate and the most unstable modes for all the simulations are listed in Table IV.1. The non-dimensional growth rate is also viewed against the core size ratio in Figure IV.14. There seems to be a higher global instabilities growth rate for

the weakly asymmetrical simulations than the symmetrical and strongly asymmetrical cases, and that it is possible that there is a critical core size ratio (given that the vortex circulation ratio is -1) at which the global instabilities growth rate is at its maximum. However, additional simulations with weakly asymmetrical core sizes should be run to confirm the correlation and identify this critical core ratio. Due to time constraints, this is not performed in the current study.

Table IV.1. Measured growth rates for most unstable wavenumber

	Most unstable mode	Growth rate
a_{01}/a_{02}= 1.00	$k^*_{max} = 1.4$	0.866
a_{01}/a_{02}= 1.05	$k^*_{max} = 1.26$	0.874
a_{01}/a_{02}= 1.10	$k^*_{max} = 1.32$	0.903
a_{01}/a_{02}= 1.15	$k^*_{max} = 1.38$	0.904
a_{01}/a_{02}= 1.25	$k^*_{max} = 1.5$	0.898
a_{01}/a_{02}= 1.50	$k^*_{max} = 1.5$	0.843
a_{01}/a_{02}= 1.75	$k^*_{max} = 1.75$	0.794

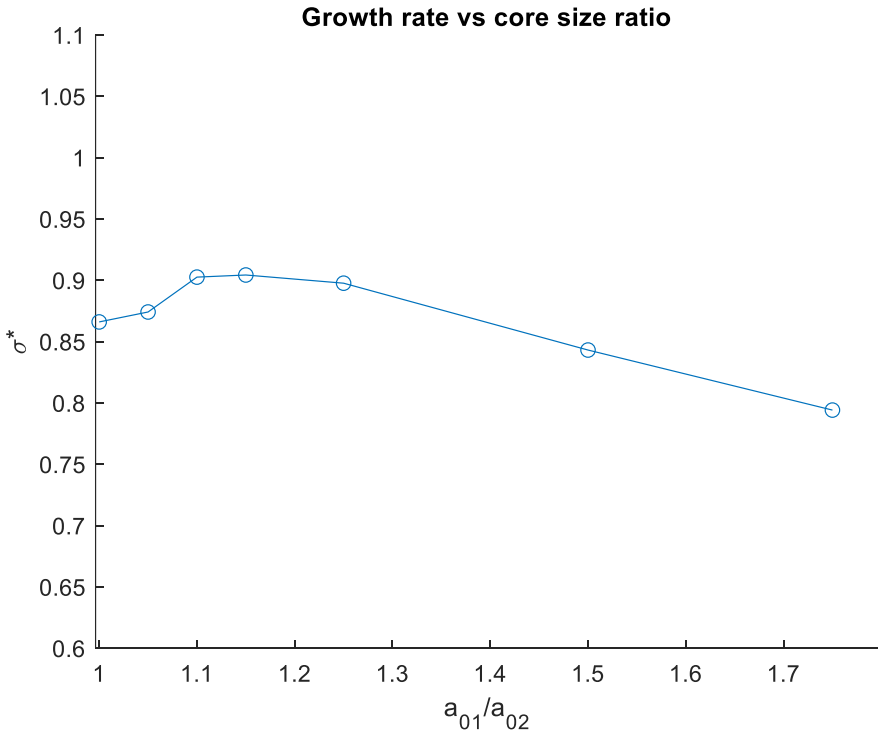

Figure IV.14: Growth rate for the most unstable mode of elliptical instability as a function of asymmetry.

IV.C Theoretical Comparison

To provide a comparison of the growth rates for the asymmetrical cases against existing literature, the theoretical growth rate of instabilities on vortices with identical parameters as those seen in this study is computed using the theoretical model that was first presented in [19] and later modified [6]. This prediction model equations for evaluating the growth rate in vortex 1 are also provided here:

$$\sigma_1 = \sqrt{\left(\frac{3}{4} - \frac{\bar{\Omega}_1}{4}\right)^4 s_0^2(\bar{\Omega}_1)\frac{\Gamma_2^2}{4\pi^2 b^4} - (\varpi^{(1)} - \bar{\Omega}_1)^2 \frac{\Gamma_1^2}{4\pi^2 a_1^4}} - \frac{\nu}{2\pi a_1^2}\varsigma^{(1)} \qquad \text{Eq. IV-9}$$

$$\bar{\Omega}_1 = \left(\frac{a_1}{b}\right)^2 \frac{\Gamma_1 + \Gamma_2}{\Gamma_1} \qquad \text{Eq. IV-10}$$

$$s_0(\bar{\Omega}) = 1.5 + 0.1323(0.32 - \bar{\Omega})^{-9/5} \qquad \text{Eq. IV-11}$$

$$\varpi^{(1)} = -0.135(ka_1 - 2.26), \quad \varsigma^{(1)} = 74.02 + 64.15(ka_1 - 2.26) \qquad \text{Eq. IV-12}$$

The growth rates of the instability in vortex 2 are obtained by exchanging the subscripts 1 and 2 in all expressions. The growth rates evaluated using the above equations are dimensional and can be nondimensionalized by using the relation $\sigma^* = \frac{\sigma}{\Gamma_0/2\pi b^2}$.

Figure IV.15 shows the theoretical growth rates of the elliptical instability of wavenumber k^*_{max} on vortex 1 and 2 along with the global instability growth rate evaluated over the entire flow field in the numerical study. The theoretical growth rates for $k^* = 1.2$ are also plotted for the symmetric case, since in the numerical simulation it had a similar global instability grow rate to $k^*_{max} = 1.4$. The growth rate from the current numerical study seems to be an average of the growth rates on the individual vortices, this is expected since the global instability growth rate accounts for the growth on both vortices.

It should be noted that the theoretical model has limitations on its applicability. For instance, the model is more suited for high Reynolds number flows ($\mathrm{Re}_\Gamma > 10^5$) as it more accurately predicts the internal strain rate from the easily-calculated external strain rate. In addition, the model assumes small aspect ratio (a/b < 0.2) to minimize effects of vorticity stripping. Despite both assumptions deviating from the conditions of the simulations, the results of the numerical study and the theoretical model are comparable.

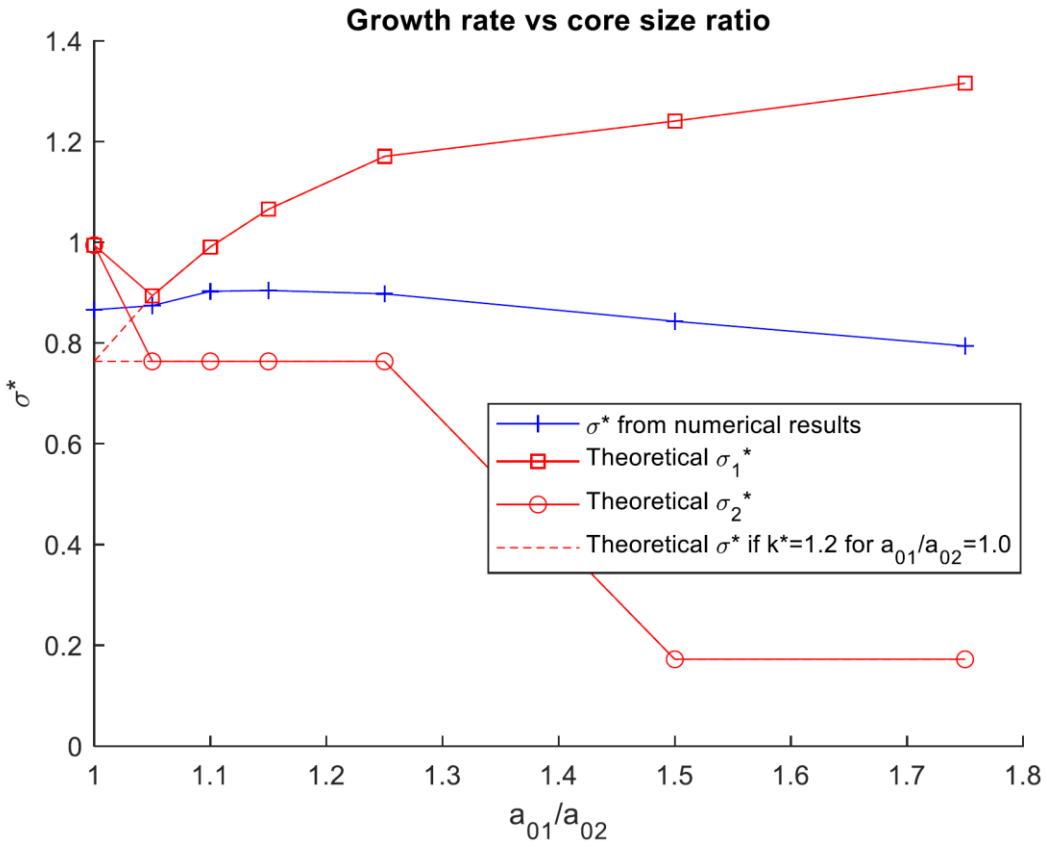

Figure IV.15: Growth rate for the most unstable mode of elliptical instability for all simulations compared against theoretical growth rate evaluated using theoretical model provided in [19] that is later modified in [6].

Chapter V Conclusions

V.A Summary

In this thesis, the behavior and growth of elliptical instability in two counter-rotating vortices with various levels of asymmetry are studied using numerical simulation. Specifically, for the instance that the initial circulation ratio of the vortices is -1, the effects of different vortex core sizes and peak vorticities on the nature of the vortex interaction and growth of the instability are examined.

In the seven simulated cases, despite the pair of vortices having equal circulation magnitudes, the vortex with the larger core size and lower peak vorticity is the weaker vortex. The perturbations grow preferentially on this weaker vortex due to the larger relative strain it experiences. Furthermore, there seems to be an optimal level of weak asymmetry (around a_{01}/a_{02}= 1.15) that would lead to the fastest growth rate for the most unstable perturbation mode. The growth rates from each of the simulations are then compared to their theoretical counterparts based on the theoretical prediction model in [19] and [6], and comparable results are found despite deviation from the theoretical model assumptions.

V.B Future Work

Though the current study offered insights into the development of the elliptical instability on a pair of unequal counter-rotating vortices in the linear phase, several points of interest remain and could be further explored in a future work.

One area of uncertainty is in the determination of the most unstable mode of elliptical instability for each simulation, especially for the cases that have similar growth rates for different wavenumbers. A linear perturbation analysis could be performed for the current simulation

parameters to provide analytical comparison for the most unstable wavenumber of the elliptical instability; it could be similarly performed for additional vortex parameters prior to simulation so that the initial condition can be prescribed to excite the most unstable mode and save computation cost.

As mentioned briefly in Section IV.C, the theoretical model predicts the instability growth rate on each vortex separately while the growth rate evaluated from the numerical results is based on the data from the entire flow field. To better compare against the theoretical prediction model formulated in [19] and [6], the growth rate of the instabilities on each individual vortex could be calculated using the vortex core displacement method.

In this study, the behavior of the elliptical instability for equal strength vortices with asymmetry in peak vorticity and core size is studied, with emphasis on the linear phase development. Due to the high computation costs of three-dimensional flows, the resolution was not refined enough to fully resolve the flow behavior in the nonlinear phase. However, late stage evolution of the elliptical instability for these vortex pairs could be investigated to confirm whether the faster linear growth rate of the elliptical instability also leads to faster overall breakdown of the primary vortices.

Finally, additional studies could be done to examine whether growth rate dependence on vortex core size ratio would be qualitatively similar if circulation ratio deviates from -1. If so, a comprehensive asymmetry parameter that accounts for variations in circulation ratio, peak vorticity ratio, and core size ratio could be developed to better predict and characterize elliptical instability growth.

References

[1] T. Leweke and C. H. K. Williamson, "Cooperative Elliptic Instability of a Vortex Pair," *Journal of Fluid Mechanics,* vol. 360, pp. 85-119, 1998.

[2] R. L. Bristol, J. M. Ortega, P. S. Marcus and Ö. Savas, "On Cooperative Instabilities of Parallel Vortex Pairs," *Journal of Fluid Mechanics,* vol. 517, pp. 331-358, 2004.

[3] S. C. Crow, "Stability Theory for a Pair of Trailing Vortices," *AIAA Journal,* vol. 8, no. 12, pp. 2172-2179, 1970.

[4] S. E. Widnall, D. Bliss and C.-Y. Tsai, "The Instability of Short Waves on a Vortex Ring," *Journal of Fluid Mechanics,* vol. 66, pp. 35-47, 1974.

[5] D. W. Moore and P. G. Saffman, "The Instability of a Straight Vortex Filament in a Strain Field," *Proc. R. Soc. Lond. A,* vol. 346, no. 1646, pp. 413-425, 1975.

[6] T. Leweke, S. Le Dizes and C. H. K. Williamson, "Dynamics and Instabilities of Vortex Pairs," *Annual Review of Fluid Mechanics,* vol. 48, pp. 507-541, 2016.

[7] S. E. Widnall, D. Bliss and A. Zalay, "Theoretical and Experimental Study of the Stability of a Vortex Pair," *Aircraft Wake Turbulence and Its Detection,* pp. 305-338, 1971.

[8] D. W. Moore and P. G. Saffman, "Axial flow in laminar trailing vortices," *Proceedings of the Royal Society,* vol. 333, no. 1595, 1973.

[9] T. Leweke and C. H. K. Williamson, "Experiments on long-wavelength instability and reconnection of a vortex pair," *Physics of Fluids,* 2011.

[10] F. Laporte and A. Corjon, "Direct Numerical Simulations of the elliptic instablity of a vortex pair," *Physics of Fluids,* vol. 12, no. 5, pp. 1016-1031, 2000.

[11] H. T. Liu, "Effects of Ambient Turbulence on the Decay of a Trailing Vortex Wake," *Journal of Aircraft,* vol. 29, pp. 255-263, 1992.

[12] W. Rojanaratanangkule and J. Tunkaew, "Direct Numerical Simulation of a Counter-Rotating Vortex Pair Embedded in Turbulence," in *Australasian Fluid Mechanics Conference,* Perth, Australia, 2016.

[13] J. F. Garten, J. Werne, D. C. Fritts and S. Arendt, "Direct Numerical Simulation of the Crow Instability and Subsequent Vortex Reconnection in a Stratified Fluid," *Journal of Fluid Mechanics,* vol. 426, pp. 1-45, 2001.

[14] R. R. Kerswell, "Elliptical Instability," *Annual Review of Fluid Mechanics,* vol. 34, pp. 83-113, 2002.

[15] F. Laporte and T. Leweke, "Elliptic Instability of Counter-Rotating Vortices: Experiment and Direct Numerical SImulation," *AIAA,* vol. 40, no. 12, pp. 2483-2494, 2002.

[16] H. Tsutsui, "Evolution of a Counter-Rotating Vortex Pair in a Stably Stratified Fluid," University of California San Diego, La Jolla, 2003.

[17] J. So, K. Ryan and G. J. Sheard, "Short-wave instabilities on a vortex pair of unequal strength circulation ratio," *Applied Mathematical Modelling,* pp. 1581-1590, 2011.

[18] J. M. Ortega, R. L. Brostol and O. Savas, "Experimental study of the instability of unequal-strenght counter-rotating vortex pairs," *Journal of Fluid Mechanics,* vol. 474, pp. 35-84, 2003.

[19] S. Le Dizès and F. Laporte, "Theoretical Predictions for the Elliptical Instability in a Two-Vortex Flow," *Journal of Fluid Mechanics,* vol. 471, pp. 169-201, 2002.

[20] C. Eloy and S. Le Dizès, "Three-dimensional Instability of the Burgers and Lamb-Oseen Vortices in a Strain Field," *Journal of Fluid Mechanics,* vol. 378, pp. 145-166, 1999.

[21] P. Orlandi, G. F. Carnevale, S. K. Lele and K. Shariff, "DNS Study of Stability of Trailing Vortices," in *Proceedings of the Summer Program, Center for Turbulence Research,* 1998.

[22] S. Rezaeiravesh, N. Jansson, A. Peplinski, J. Vincent and P. Schlatte, Editors, "Nek5000, Theory, Implementation and Optimization," Stockholm, 2021.

[23] G. E. Karniadakis, M. Israeli and S. A. Orszag, "High-order splitting methods for the incompressible navier-stokes equations," *Journal of Computational Physics,* vol. 97, no. 2, pp. 414-443, 1991.

[24] J. C. R. Hunt, A. A. Wray and P. Moin, "Eddies, streams, and convergence zones in turbulent flows," *Center for Turbulence Research Proceedings of the Summer Program,* vol. 1, pp. 193-208, 1988.

[25] D. Fabre, L. Jacquin and A. Loof, "Optimal perturbations in a four-vortex aircraft wake in a counter-rotating configuration," *Journal of Fluid Mechanics,* vol. 451, pp. 319-328, 2002.

[26] G. E. Karniadakis, M. Israeli and S. A. Orszag, "High-order splitting methods for the incompressible Navier-Stokes equations," *Journal of Computational Physics,* vol. 97, no. 2, pp. 414-443, 1991.